Presupernova Evolution of Rotating Massive Stars I: Numerical Method and Evolution of the Internal Stellar Structure

A. Heger[1,2], N. Langer[2,3],
and
S. E. Woosley[1,2]

ABSTRACT

The evolution of rotating stars with zero-age main sequence (ZAMS) masses in the range $8\,\mathrm{M}_\odot$ to $25\,\mathrm{M}_\odot$ is followed through all stages of stable evolution. The initial angular momentum is chosen such that the star's equatorial rotational velocity on the ZAMS ranges from zero to $\sim 70\,\%$ of break-up. The stars rotate rigidly on the ZAMS as a consequence of angular momentum redistribution during the pre-main sequence evolution. Redistribution of angular momentum and chemical species are then followed as a consequence of Eddington-Sweet circulation, the Solberg-Høiland instability, and secular and dynamic shear instability. The effects of the centrifugal force on the stellar structure are included. Convectively unstable zones are assumed to tend towards rigid rotation and uncertain mixing efficiencies are gauged by observations. We find, as noted in previous work, that rotation increases the helium core masses and enriches the stellar envelopes with products of hydrogen burning. We determine, for the first time, the angular momentum distribution in typical presupernova stars along with their detailed chemical structure. Angular momentum loss due to (non-magnetic) stellar winds and the redistribution of angular momentum during core hydrogen burning are of crucial importance for the specific angular momentum of the core. Neglecting magnetic fields, we find angular momentum transport from the core to the envelope to be unimportant after core helium burning. We obtain specific angular momenta for the iron core and overlaying material of $10^{16}\ldots10^{17}\,\mathrm{erg\,s}$. These values are insensitive to the initial angular momentum and to uncertainties in the efficiencies of rotational mixing. They are small enough to avoid triaxial deformations of the iron core before it collapses, but could lead to neutron stars which rotate close to break-up. They are also in the range required for the collapsar model of gamma-ray bursts. The apparent discrepancy with the measured rotation rates of young pulsars is discussed.

Subject headings: stars: rotation, supernovae, nucleosynthesis – pulsars – hydrodynamics – methods: numerical

[1]Astronomy and Astrophysics Department, University of California, Santa Cruz, CA 95064
[2]Max-Planck-Institut für Astrophysik, Karl-Schawarzschild-Straße 1, 85740 Garching, Germany
[3]Institut für Physik, Am Neuen Palais 10, 14469 Potsdam, Germany

1. Introduction

The quantitative theory of stellar structure is more than 100 years old (see, e.g., Emden 1907) and our understanding of the stellar interior has improved dramatically during this time, especially since it became possible to construct detailed stellar models with the help of computers in the 1950's. However, even today, our understanding of many observable properties of massive stars ($M_{\rm ZAMS} \gtrsim 8\mathrm{M}_\odot$, $\log L/\mathrm{L}_\odot \gtrsim 4$) remains rudimentary.

Aside from comparatively minor uncertainties remaining in the opacities and nuclear physics, the major frontiers in the study of stars, and indeed stellar evolution in general, are proper treatments of convection, mass loss, and rotation. This paper is the first in a series concerning the effects of rotation and angular momentum transport on the evolution of stars massive enough that a single one can become a supernova ($M \gtrsim 8\,\mathrm{M}_\odot$).

The first to recognize the importance of rotation for celestial bodies was Sir Isaac Newton. Early studies of rotating, self-gravitating, incompressible fluids were carried out by McLaurin, Jakobi, Poincaré, and Schwarzschild. Additional important contributions to the numerical treatment of rotating stars were provided by Kippenhahn & Thomas (1970). Kippenhahn et al. (1970) performed calculations taking these effects into account using a simple model for angular momentum transport. Studies with artificial rotation laws were carried out by Endal & Sofia (1976). In their pioneering work, Endal & Sofia (1978) considered several rotationally induced instabilities, made order-of-magnitude estimates for their efficiencies, and performed time-dependent stellar evolution calculations of rotating massive stars up to the ignition of carbon burning. Later, Pinsonneault et al. (1989) introduced a parameterization of the poorly known efficiencies of the rotationally induced transport processes of Endal & Sofia (1978) and gauged them to solar models. The formalism we shall employ here is based largely upon these two works. We differ, however, in using more recent data to calibrate the uncertain efficiencies for angular momentum and composition transport in this formalism and especially in following the stars past carbon burning, all the way to the presupernova state.

Our formalism (discussed in detail, in §2) is relatively simple compared to others used in recent studies of rotation during hydrogen and helium burning, e.g., Langer (1992), Denissenkov (1994), Eryurt et al. (1994), Chaboyer & Zahn (1992), Zahn (1992), Urpin et al. (1996), Talon et al. (1997), Meynet (1997), and Maeder & Zahn (1998), but easier to understand and implement, and more easily extrapolable to the late stages of stellar evolution. Indeed our poor understanding, especially during the late stages of stellar evolution, of both convection and possible modifications to angular momentum transport by magnetic fields (not considered in the present work nor in the papers cited above) suggests that it is worth trying something simple first.

Most of the rotation physics described in Sect. 2 can already be found, with slight modifications, in previous papers. However, since this is the first in a series of papers, it will facilitate our presentation to have all the relevant equations collected in one place. We also correct several errors. In previous publications, e.g. in the equation for the secular shear instability, and cast the results in a consistent notation.

Following a summary of how we model various rotationally induced instabilities (Sect. 2) and a discussion of the uncertain parameters of the model (Sect. 3), we discuss the implementation of this physics in the stellar codes in Sect. 4 and give an overview of the initial models in Sect. 5. The evolution during hydrogen burning and helium burning is discussed in Sections 6 and 7, respectively. In Sect. 8 we compare our results to the works of other authors. The late evolution is discussed in Sect. 9 and the final angular momentum distribution at the presupernova stage is given in Sect. 10. Its implications are discussed in Sect. 11 and a summary and our conclusions are given in Sect. 12.

Discussion of the details of observable parameters (evolution in the HR diagram, surface abundances, lifetimes) and presupernova nucleosynthesis are deferred to future papers.

2. Rotation and Mixing in Massive Stars

2.1. Modification to the stellar structure equations

In rotating stars, centrifugal forces act on the matter and lead to deviations from spherical symmetry. For slow to moderate rotation these deformations remain rotationally symmetric (Tassoul 1978). Only if the rotational energy exceeds a notable fraction of the binding energy of the star does genuine triaxial deformation result.

In this work we consider only the case of "slow" rotation, i.e., where no triaxial deformations are expected. Some stars may reach "critical" rotation velocity (Sect. 2.6) at their surfaces during brief stages of their evolution (Heger & Langer 1998). However, except for possibly modifying the mass loss rate (Sect. 2.6), this affects only the very outermost layers and is not expected to have a big influence on the results of this paper.

Even for slow rotation, the shapes of surfaces of constant pressure, constant density, and constant temperature are affected by the centrifugal potential and thus deviate from spherical symmetry. The momentum equation and the energy transport equation for spherically symmetric stars must be modified to take this effect into account.

In this work, the centrifugal force is included following Kippenhahn & Thomas (1970) in the approximation of Endal & Sofia (1976) and applied to the hydrodynamic stellar structure equations (Fliegner 1993). In this approach, mass shells correspond to isobars instead of spherical shells. Corrections are applied to the acceleration and the radiative temperature gradient. According to Zahn (1975), Chaboyer & Zahn (1992), and Zahn (1992), anisotropic turbulence acts much stronger on isobars than in the perpendicular direction. This enforces "shellular" rotation rather than cylindrical rotation (Meynet & Maeder 1997), and it sweeps out compositional differences on isobars. Therefore it can be assumed that matter on isobars is approximately chemically homogeneous. Together with the shellular rotation this allows us to retain a one-dimensional approximation. The specific angular momentum, j, of a mass shell is treated as a local variable and the angular velocity, ω, is computed from the specific moment of inertia, i. The time-dependent angular momentum redistribution is discussed in Sect. 2.5, and its influence on transport processes in Sect. 2.3. We begin here by describing the modification to the stellar structure equations of non-rotating stars (see also Endal & Sofia 1976; Meynet & Maeder 1997).

Let V_{P} be the volume enclosed by a surface of constant pressure, P, and $S_{\mathrm{P}} := \partial V_{\mathrm{P}}$ its surface area. Then its "radius", r_{P}, is defined as the radius of a sphere of the same volume, $V_{\mathrm{P}} = 4\pi r_{\mathrm{P}}{}^3/3$, and the equation of continuity becomes

$$\left(\frac{\partial m_{\mathrm{P}}}{\partial r_{\mathrm{P}}}\right)_t = 4\pi r_{\mathrm{P}}{}^2 \rho \ , \qquad (1)$$

where ρ is the density and m_{P} the mass enclosed by S_{P}. For quantities varying on isobars, a mean value is defined by

$$\langle\,\cdot\,\rangle := \frac{1}{S_{\mathrm{P}}} \oint_{S_{\mathrm{P}}} \cdot \ \mathrm{d}\sigma \ , \qquad (2)$$

where $\mathrm{d}\sigma$ is an element of isobaric surface area. The effective gravitational acceleration $\mathbf{g}$ is normal to S_{P}. For the equation of momentum balance, one finds (Endal & Sofia 1976)

$$\left(\frac{\partial P}{\partial m_{\mathrm{P}}}\right)_t = -\frac{G m_{\mathrm{P}}}{4\pi r_{\mathrm{P}}{}^4} f_{\mathrm{P}} - \frac{1}{4\pi r_{\mathrm{P}}{}^2}\left(\frac{\partial^2 r_{\mathrm{P}}}{\partial t^2}\right)_{m_{\mathrm{P}}} \ , \qquad (3)$$

where G is the gravitational constant, P, the pressure, t, the time, and the inertia term (last term) is added here. The influence of rotation is described by the quantity f_{P}

$$f_{\mathrm{P}} := \frac{4\pi r_{\mathrm{P}}{}^4}{G m_{\mathrm{P}} S_{\mathrm{P}}} \langle g^{-1}\rangle^{-1} \ , \qquad (4)$$

where $g := |\mathbf{g}|$. The radiative temperature gradient then takes the form

$$\left(\frac{\partial \ln T}{\partial \ln P}\right)_t = \frac{3\kappa}{16\pi a c G}\frac{P}{T^4}\frac{L_{\mathrm{P}}}{m_{\mathrm{P}}}\frac{f_{\mathrm{T}}}{f_{\mathrm{P}}}\left[1 + \frac{r_{\mathrm{P}}{}^2}{G m_{\mathrm{P}} f_{\mathrm{P}}}\left(\frac{\partial^2 r_{\mathrm{P}}}{\partial t^2}\right)_{m_{\mathrm{P}}}\right]^{-1} , \qquad (5)$$

where κ is the opacity, T the temperature, a the radiation constant, and L_{P}, the energy flux through S_{P}. The last factor on the right hand side is included to account for inertia as it follows from the momentum equation (Fliegner 1993), and

$$f_{\mathrm{T}} := \left(\frac{4\pi r_{\mathrm{P}}{}^2}{S_{\mathrm{P}}}\right)^2 \left(\langle g\rangle\langle g^{-1}\rangle\right)^{-1} . \qquad (6)$$

For the derivation of these formulae and for a numerical evaluation of f_{T} and f_{P}, see Endal & Sofia (1976). The equations for f_{T} and f_{P} are solved iteratively with the stellar structure equations in order to obtain consistent models (Endal & Sofia 1976; Fliegner 1993). In the rest of this work, the subscript P is omitted (except for f_{P}).

There is, in principle, an inconsistency between the assumption of shellular rotation and the method described by Kippenhahn & Thomas (1970), i.e., the assumption of shellular rotation does not generally lead to a conservative potential as it does for a constant rotation rate on cylinders, which is used by Kippenhahn & Thomas (1970). However, Meynet & Maeder

(1997) show that replacing the average $\langle \cdot \rangle$ by "appropriate mean values", i.e., reinterpreting the quantities describing the stellar structure as the mean values over the isobars, allows one to keep the formalism of Kippenhahn & Thomas (1970) as a good approximation.

2.2. Ordinary mixing in the absence of rotation

Compositional mixing is generally treated as a diffusive process and implemented by solving the diffusion equation

$$\left(\frac{\partial X_n}{\partial t}\right)_m = \left(\frac{\partial}{\partial m}\right)_t \left[(4\pi r^2 \rho)^2 D \left(\frac{\partial X_n}{\partial m}\right)_t\right] + \left(\frac{\mathrm{d} X_n}{\mathrm{d}t}\right)_{\mathrm{nuc}} , \tag{7}$$

where D is the diffusion coefficient constructed from the sum of individual mixing processes and X_n, the mass fraction of species n. The second term on the right hand side accounts for nuclear reactions. At the inner and outer boundary reflecting conditions are used:

$$\left(\frac{\partial X_n}{\partial m}\right)_t \Bigg|_{m=0} = 0 = \left(\frac{\partial X_n}{\partial m}\right)_t \Bigg|_{m=M(t)} . \tag{8}$$

Mixing, burning, and mass loss are treated as separate, sequential operations. The different contributions to the diffusion coefficient, D, are discussed in the following sections.

2.2.1. Convection and overshooting

Convection occurs when the temperature gradient exceeds the adiabatic condition, as modified by any gradient in mean molecular weight, μ (Fig. 1). That is, a stratification is stable against convection if

$$\nabla_{\mathrm{ad}} - \nabla + \frac{\varphi}{\delta}\nabla_\mu \geq 0 \tag{9}$$

(e.g., Kippenhahn & Weigert 1991). This is the so-called Ledoux criterion for convection. Here the common definitions are used:

$$\nabla_{\mathrm{ad}} := \left(\frac{\partial \ln T}{\partial \ln P}\right)_{\mathrm{ad}} , \quad \nabla_\mu := \frac{\mathrm{d}\ln \mu}{\mathrm{d}\ln P} , \quad \nabla := \frac{\mathrm{d}\ln T}{\mathrm{d}\ln P} , \tag{10}$$

$$\delta := -\left(\frac{\partial \ln \rho}{\partial \ln T}\right)_{\mu,P} , \qquad \varphi := \left(\frac{\partial \ln \rho}{\partial \ln \mu}\right)_{P,T} . \tag{11}$$

The index "ad" stands here for "at constant entropy *and* composition".

The diffusion coefficient for composition mixing is treated according to the mixing-length theory (Vitense 1953; Böhm-Vitense 1958):

$$D_{\mathrm{conv}} := \alpha_{\mathrm{MLT}} H_{\mathrm{P}} v_{\mathrm{conv}}/3 , \tag{12}$$

where v_{conv} is the convective velocity. The pressure scale-height is defined for the hydrostatic case by

$$H_{\mathrm{P}} := -\frac{\mathrm{d}r}{\mathrm{d}\ln P} = \frac{P}{\rho g} . \tag{13}$$

The local gravitational acceleration is given by $g = Gm/r^2$. In this work a mixing-length parameter of $\alpha_{\mathrm{MLT}} = 1.5$ (Langer 1991) is used.

The mixing performed by convection is fast in comparison to most of the other time-scales relevant for the stellar evolution. It operates on the local dynamical time-scale and usually manages to smooth out any compositional inhomogeneities in the regions where it is active. Only when the time-scale of thermonuclear burning becomes comparable to that of convection, as, e.g., during central silicon and shell oxygen burning, can notable gradients persist.

In the present work "overshooting" of the convection into the convectively stable regime defined by Eq. (9) is neglected. It will be shown that rotation leads to mixing above the convective core of massive stars during central hydrogen burning and thereby to the formation of more massive helium cores later in the evolution. In order to obtain such mixing, large overshooting is often introduced in literature (e.g., Chin & Stothers 1991; Schaller et al. 1992), but moderate rotation can lead to similar effects.

2.2.2. Semiconvection

Semiconvection is a secular instability which can occur in non-rotating stars. According to a local, linear stability analysis by Kato (1966), it is an oscillatory instability which appears in regions where an unstable temperature gradient is stabilized against convection by a sufficiently large gradient in the mean molecular weight (μ-gradient), i.e., it lives in the regime

$$\frac{\varphi}{\delta}\nabla_\mu \geq \nabla - \nabla_{\mathrm{ad}} \geq 0 \tag{14}$$

(Kippenhahn & Weigert 1991; and Fig. 1). Heat transfer between a displaced mass element and its surrounding causes the growth of the instability on the local thermal time-scale.

In the code STERN (see Sect. 4.1), semiconvection is treated following Langer et al. (1983). The diffusion coefficient for this process is computed from

$$D_{\mathrm{sem}} = \frac{\alpha_{\mathrm{sem}} K}{6 c_{\mathrm{P}} \rho} \frac{\nabla - \nabla_{\mathrm{ad}}}{\nabla_{\mathrm{ad}} - \nabla + \frac{\varphi}{\delta}\nabla_\mu} \ , \quad K = \frac{4acT^3}{3\kappa\rho} \ , \tag{15}$$

where K is the thermal conductivity and c_{P} the specific heat at constant pressure. As proposed by Langer (1991), an efficiency parameter of $\alpha_{\mathrm{sem}} = 0.04$ is adopted here.

In KEPLER (see Sect. 4.2) semiconvection is computed from (Weaver et al. 1978; Weaver & Woosley 1993)

$$D'_{\mathrm{sem}} = \frac{1}{6} {\alpha_{\mathrm{MLT}}}^2 v_{\mathrm{sem}} H_{\mathrm{P}} \ , \tag{16}$$

where the velocity v_{sem} is determined through

$$v_{\mathrm{sem}} = \sqrt{(\nabla - \nabla_{\mathrm{ad}}) \frac{P\delta}{g\rho^2} \frac{\mathrm{d}P}{\mathrm{d}r}} \ . \tag{17}$$

The diffusion coefficient is limited to a fraction α_{sem} of the radiative diffusion coefficient

$$D_{\mathrm{rad}} = \frac{K}{\rho c_{\mathrm{V}}} \tag{18}$$

by means of

$$D_{\mathrm{sem}} = \frac{\alpha_{\mathrm{sem}} D_{\mathrm{rad}} D'_{\mathrm{sem}}}{D'_{\mathrm{sem}} + \alpha_{\mathrm{sem}} D_{\mathrm{rad}}} \ . \tag{19}$$

As usual, c_{V} denotes the specific heat at constant volume. In this work a value of $\alpha_{\mathrm{sem}} = 10^{-4}$ is used in KEPLER, which results in a comparable efficiency for semiconvection as the value used for STERN (Woosley 1997).

2.3. Rotationally induced mixing

In this work, the mixing processes discussed in Endal & Sofia (1978) are included in a parametric way, following the work of Pinsonneault et al. (1989). Five different processes are considered. To account for the uncertain mixing efficiency of each, they are weighed by efficiency factors (Pinsonneault et al. 1989; Sect. 3) and then added to the diffusion coefficient, D, in the diffusion equation (7).

2.3.1. Dynamical shear instability

Dynamical shear instability occurs when the energy that can be gained from the shear flow becomes comparable to the work that has to be done against the gravitational potential for the adiabatic turn-over of a mass element ("eddy"). This means that it is stabilized by density gradients. Since there is no work required to mix on isobars, this instability can work very efficiently on those (horizontal turbulence; Zahn 1992) and thus enforce rigid rotation horizontally (Endal & Sofia 1978; Pinsonneault et al. 1989). Thus chemical inhomogeneities are smoothed on isobars. This, together with the so called baroclinic instability, which also acts barotropic for shear on isobars on a dynamical time scale (Zahn 1983), justifies the assumption of shellular rotation and that the composition is only a function of the isobars (Sect. 2.1).

The linear condition for stability is given by

$$R_{\mathrm{i}} := \frac{\rho\delta}{P}\left(\nabla_{\mathrm{ad}} - \nabla + \frac{\varphi}{\delta}\nabla_\mu\right)\left(g\frac{\mathrm{d}\ln r}{\mathrm{d}\omega}\right)^2 > R_{\mathrm{i,c}} \approx \frac{1}{4} \tag{20}$$

for the case of a rotating fluid (Zahn 1974). Here, ω is the angular velocity, R_{i}, Richardson number, and $R_{\mathrm{i,c}}$, its critical value, about 1/4. Note that the term for ∇_μ in Eq. (20) was omitted in the original work by Endal & Sofia (1978) and Pinsonneault et al. (1989). The corresponding diffusion coefficient is computed from the spatial extent of the unstable region d_{inst}, limited to a pressure scale-height, and the local dynamical time-scale (see also Endal & Sofia 1978):

$$D_{\mathrm{DSI}} = \left[\min\{d_{\mathrm{inst}}, H_{\mathrm{P}}\}\left(1 - \max\left\{\frac{R_{\mathrm{i}}}{R_{\mathrm{i,c}}}, 0\right\}\right)\right]^2 / \tau_{\mathrm{dyn}} \ , \tag{21}$$

where the dynamical time-scale is defined by

$$\tau_{\mathrm{dyn}} := \sqrt{r^3/(Gm)} \ . \tag{22}$$

Furthermore, it is assumed that the instability is weaker when the deviation from the Richardson criterion is smaller. This is accounted for by a factor $(1 - R_{\mathrm{i,c}}/R_{\mathrm{i}})^2$, which is limited to the range $[0, 1]$. For $R_{\mathrm{i}} > R_{\mathrm{i,c}}$, the flow is assumed to be stable against the dynamical shear instability and thus D_{DSI} is set to 0.

2.3.2. Solberg-Høiland instability

The Solberg-Høiland instability arises if an adiabatically displaced mass element experiences a net force (the sum of gravity, buoyancy and centrifugal force) that has components in the direction of the displacement only. Wasiutyński (1946) gives a condition for the stability against axisymmetric adiabatic perturbations of this kind. It separates into two scalar conditions. At the equator the condition for stability in the vertical direction is

$$R_{\mathrm{SH}} := \frac{g}{\rho}\left[\left(\frac{\mathrm{d}\rho}{\mathrm{d}r}\right)_{\mathrm{ad}} - \frac{\mathrm{d}\rho}{\mathrm{d}r}\right] + \frac{1}{r^3}\frac{\mathrm{d}}{\mathrm{d}r}\left(r^2\omega\right)^2 \geq 0 \quad (23)$$

(Tassoul 1978; Endal & Sofia 1978). If the specific angular momentum $j \sim r^2\omega$ is constant with r, the last term on the left-hand side vanishes and the Ledoux criterion results — not the Schwarzschild criterion as stated by Endal & Sofia (1978). This can be seen by rewriting the condition for stability

$$R_{\mathrm{SH}} := \frac{g\delta}{H_{\mathrm{P}}}\left[\nabla_{\mathrm{ad}} - \nabla + \frac{\varphi}{\delta}\nabla_\mu\right] + \frac{1}{r^3}\frac{\mathrm{d}}{\mathrm{d}r}\left(r^2\omega\right)^2 \geq 0 \quad (24)$$

and comparing it with Eq. (9). If, on the other hand, the medium is marginally stable to convection, the first term on the right hand side vanishes and the Rayleigh criterion results (Tassoul 1978; Kippenhahn & Weigert 1991). Note that this instability only occurs in regions of *decreasing* specific angular momentum (Fig. 3) and is strongly suppressed in stable stratifications ($\nabla < \nabla_{\mathrm{ad}} + \frac{\varphi}{\delta}\nabla_\mu$).

The diffusion coefficient resulting from the Solberg-Høiland instability is estimated in a way similar to that for the dynamical shear instability. The extent of the unstable region, d_{inst}, limited to the pressure scale-height, is used as the characteristic length-scale, and the dynamical time-scale is used as characteristic time-scale:

$$D_{\mathrm{SHI}} = \left[\min\left\{d_{\mathrm{inst}}, H_{\mathrm{P}}\right\}\left(\frac{r\,R_{\mathrm{SH}}}{g}\right)\right]^2 / \tau_{\mathrm{dyn}}\ . \quad (25)$$

Again, as for the dynamical shear instability, a factor of order unity $(r\,R_{\mathrm{SH}}/g)$ was introduced to smoothly turn on the instability as the criterion for stability gets increasingly violated, and D_{SHI} is set to 0 wherever the stability criterion is fulfilled.

2.3.3. Secular shear instability

The strict criterion for dynamical shear instability can be relaxed considerably by allowing for thermal adjustment of radial perturbations. However, this process then operates only on a thermal time-scale, and is therefore a secular process. Gradients in the mean molecular weight, which may inhibit the occurrence of the instability, also have to be taken into account.

According to Endal & Sofia (1978), the following two conditions have to be violated simultaneously for this instability to set in (Fig. 1):

$$R_{\mathrm{is},1} := \frac{\mathcal{P}_{\mathrm{r}}\,R_{\mathrm{e,c}}}{8}\frac{\rho\delta}{P}(\nabla_{\mathrm{ad}} - \nabla)\left(g\frac{\mathrm{d}\ln r}{\mathrm{d}\omega}\right)^2 > R_{\mathrm{i,c}} \quad (26)$$

(Townsend 1958; Zahn 1975) because of the relaxed condition for the temperature gradient, and

$$R_{\mathrm{is},2} := \frac{\rho\varphi\nabla_\mu}{P}\left(g\frac{\mathrm{d}\ln r}{\mathrm{d}\omega}\right)^2 > R_{\mathrm{i,c}} \quad (27)$$

since the condition for the μ-gradient is not relaxed. The latter formula follows from the physical arguments of Endal & Sofia (1978), but corrects an error in their Eq. (10). For the critical Reynolds number, $R_{\mathrm{e,c}}$, a value of 2500 is assumed in this work (but see also Richard & Zahn 1999). The Prandtl number, $\mathcal{P}_{\mathrm{r}}$, is defined as the ratio of the thermal diffusion time-scale to the angular momentum diffusion time-scale, and is estimated according to Tassoul (1978):

$$\mathcal{P}_{\mathrm{r}} = \frac{c_{\mathrm{V}}(\mu_{\mathrm{p}} + \mu_{\mathrm{r}})}{\chi}\ , \quad (28)$$

where the coefficients of shear viscosity of the plasma and by radiation are computed according to

$$\mu_{\mathrm{p}} \approx 0.406\,\frac{\sqrt{m_{\mathrm{i}}(k_{\mathrm{B}}T)^5}}{(Z_{\mathrm{i}}e)^4\ln\Lambda}\ , \qquad \mu_{\mathrm{r}} = \frac{4aT^4}{15c\kappa\rho} \quad (29)$$

(Spitzer 1962; Tassoul 1978), respectively. The quantity Λ is the ratio of the cut-off length for ion collisions, which is taken as the ratio of the Debye length, to the impact parameter for a $\pi/2$ deflection for Rutherford scattering of the ions, i.e.,

$$\Lambda = \frac{2}{3e^3}\sqrt{\frac{m_{\mathrm{i}}(k_{\mathrm{B}}T)^3}{\pi\rho{Z_{\mathrm{i}}}^5}} \quad (30)$$

(for details, see Spitzer 1962). Here, e is the charge of the electron in e.s.u., c the velocity of light, k_{B} Boltzmann's constant, Z_{i} the charge number of the ion, and m_{i} its mass. It should be noted that for burning phases beyond hydrogen burning, as well as for helium, carbon, or oxygen stars, it is important to take the Z_{i}-dependence of the plasma viscosity into account. The quantity Λ enters only logarithmically and $\ln\Lambda$ is ~ 25. At temperatures below the Fermi temperature, depending somewhat on the chemical composition, the ion viscosity dominates over the electron contribution. For the evaluation of the formulae above, complete ionization is assumed.

If magnetic fields and neutrinos are neglected, the thermal conductivity is given by $\chi \approx K$ (Eq. (15); Tassoul 1978). The opacity, κ, used in this work takes into account the energy transport by radiation as well as heat conduction by degenerate electrons. Following Endal & Sofia (1978), the circulation velocity associated with this process is computed from the time-scale and the length-scale of the turbulent elements,

$$v_{\rm SSI} = \sqrt{\frac{\nu}{R_{\rm e,c}} \frac{{\rm d}\omega}{{\rm dln}\, r}} \,, \tag{31}$$

limited to the adiabatic sound velocity, $c_{\rm s}$. The kinematic viscosity, ν, is given by (Tassoul 1978)

$$\nu = \frac{\mu_{\rm p} + \mu_{\rm r}}{\rho} \,. \tag{32}$$

For the typical length-scale the velocity scale height of the flow is assumed,

$$H_{\rm v,SSI} := \left| \frac{{\rm d}r}{{\rm dln}\, v_{\rm SSI}} \right| \,, \tag{33}$$

limited to the pressure scale height. The resulting diffusion coefficient is given by

$$D_{\rm SSI} = \min\left\{v_{\rm SSI}, c_{\rm s}\right\} \min\left\{H_{\rm v,SSI}, H_{\rm P}\right\} \left(1 - \frac{\max\left\{R_{\rm is,1}, R_{\rm is,2}\right\}}{R_{\rm i,c}}\right)^2 \,. \tag{34}$$

Again, the instability is smoothly turned on with increasing violation of the stability criteria (term in the last bracket).

In recent work, Maeder & Meynet (1996),Maeder (1997a), and Maeder & Zahn (1998) reconsidered the interaction of thermal diffusivity, horizontal turbulence (due to the baroclinic instability), and vertical shear. An important conclusion that can be drawn from their work is that μ-gradients might not completely suppress the occurrence of the shear instability, since the medium is already turbulent due to the baroclinic instability. Consequently, some mixing can occur (Maeder 1997a). In the present work, we parameterize the efficiency of the secular shear instability for chemical mixing and of the μ-gradients in suppressing its occurrence (Sect. 3).

2.3.4. Eddington-Sweet circulation

As first shown by von Zeipel (1924a,b) for rigid rotation, and later by Baker & Kippenhahn (1959) for a general rotation law, a rotating star cannot be in hydrostatic and radiative thermal equilibrium at the same time. This is so because surfaces of constant temperature and constant pressure do not coincide. Consequently, large-scale circulations develop. Since inhomogeneities on isobars are quickly smoothed out by the horizontal turbulence only the perpendicular ($\approx$ radial) component of the circulation velocity is considered here, and the process is approximated by diffusion along the radial coordinate.

Kippenhahn (1974) estimated the circulation velocity as

$$v_{\rm e} := \frac{\nabla_{\rm ad}}{\delta\left(\nabla_{\rm ad} - \nabla\right)} \frac{\omega^2 r^3 l}{(Gm)^2} \left(\frac{2(\varepsilon_{\rm n} + \varepsilon_\nu) r^2}{l} - \frac{2r^2}{m} - \frac{3}{4\pi\rho r}\right) \,. \tag{35}$$

In the presence of μ-gradients, meridional circulation has to work against the potential and thus might be inhibited or suppressed (Mestel 1952, 1953). Formally, this can be written as a "stabilizing" circulation velocity,

$$v_\mu := \frac{H_{\rm P}}{\tau^*_{\rm KH}} \frac{\varphi \nabla_\mu}{\delta\left(\nabla - \nabla_{\rm ad}\right)} \tag{36}$$

(Kippenhahn 1974; Pinsonneault et al. 1989), where

$$\tau^*_{\rm KH} := \frac{Gm^2}{r(l - m\varepsilon_\nu)} \tag{37}$$

is the local Kelvin-Helmholtz time-scale, used here as an estimate for the local thermal adjustment time-scale of the currents (Pinsonneault et al. 1989). The spatial extent of the currents is typically of the order of the radius coordinate r. Here, neutrino losses are taken into account, because they reduce the thermal time-scale in the late stages of the stellar evolution significantly. Note that ε_ν is defined as the energy *generation* rate due to neutrino losses and therefore is negative. This increases the numerator in the definition of the local Kelvin-Helmholtz time-scale and thus decreases $\tau^*_{\rm KH}$.

For the evaluation of the diffusion coefficient, the sign of the circulation velocity does not matter, but the stabilizing "currents" due to μ-gradients always point in the direction opposite to the meridional flow, thus resulting in a reduction of the effective circulation velocity. The velocity is then computed from

$$v_{\rm ES} := \max\left\{|v_{\rm e}| - |v_\mu|, 0\right\} \tag{38}$$

(Endal & Sofia 1978; and Fig. 4). The diffusion coefficient is calculated as the the product of the circulation velocity and a typical length-scale for the circulation. This is assumed to be the minimum of the extent $d_{\rm inst}$ of the instability and the velocity scale-height

$$H_{\rm v,ES} := \left| \frac{\mathrm{d}r}{\mathrm{d}\ln v_{\rm ES}} \right| \tag{39}$$

(Endal & Sofia 1978), i.e.,

$$D_{\rm ES} := \min\{d_{\rm inst}, H_{\rm v,ES}\} v_{\rm ES} \ . \tag{40}$$

In recent work, Chaboyer & Zahn (1992); Zahn (1992); Urpin et al. (1996); Talon et al. (1997); Maeder & Zahn (1998) have discussed several improvements to the theory of meridional circulation and its interaction with the baroclinic instability. In contrast to the present work, their method requires the solution of a fourth order differential equation in ω, which is numerically very involved. So far this method has only been used to investigate main sequence stars. An interesting result of these work for the Eddington-Sweet circulation is that the stabilizing effect of μ-gradients, entering through $v_{\rm e}$ in $v_{\rm ES}$ (Eqs. (35) and (38)), may be reduced (Sect. 3). The second important change to the above estimate is that the interaction of the baroclinic instability and the large-scale meridional reduces the mixing efficiency of the Eddington-Sweet circulation in agreement with the numerical studies by Pinsonneault et al. (1989) for the sun. We consider these effects when we perform an empirical calibration of the mixing efficiencies in Sect. 3.

2.3.5. Goldreich-Schubert-Fricke instability

Goldreich & Schubert (1967) and Fricke (1968) performed an analysis of stability against axisymmetric perturbations (GSF instability). For the inviscid limit ($\mathcal{P}_{\rm r} \ll 1$), which can be well assumed in the interior of stars, they derive two conditions for stability in chemically homogeneous stars (Kippenhahn 1969):

$$\frac{\partial j}{\partial r} \geq 0 \qquad \text{and} \qquad \frac{\partial \omega}{\partial z} = 0 \ . \tag{41}$$

The first condition is the secular analogue to the Solberg-Høiland stability criterion Eq. (24), where the stabilization by the temperature gradient is removed due to thermal conduction. This is similar to the relation between the secular and the dynamical shear instability. The second condition in Eq. (41) is the analogue to the Taylor-Proudman theorem for slowly rotating incompressible fluids (Kippenhahn 1974; Tassoul 1978). If the rotational velocity depends on the distance from the equatorial plane, i.e., the rotation profile is not conservative, meridional flows will be driven. Also in this case, the buoyancy force, which acts to suppress the instability, can be removed by heat conduction. However, this occurs only on a thermal time-scale. Interestingly, the typical velocities for both the above processes are quite similar (Kippenhahn 1974).

Since the second condition of Eq. (41) is in general in contradiction with the shellular rotation law enforced by the baroclinic instability, except for the case of solid body rotation, the GSF instability will tend to enforce uniform rotation in chemically homogeneous regions (Endal & Sofia 1978).

The dependence of the GSF instability on differential rotation is stronger than that of Eddington-Sweet circulation, and the large-scale circulation velocity in the equatorial plane can be estimated by

$$v_{\rm g} = \frac{2H_{\rm T}r}{{H_{\rm j}}^2}\left(1+2\frac{\mathrm{d}\ln r}{\mathrm{d}\ln\omega}\right)^{-1} v_{\rm e} = \frac{2H_{\rm T}}{H_{\rm j}}\,\frac{\mathrm{d}\ln\omega}{\mathrm{d}\ln r} v_{\rm e} \tag{42}$$

(Endal & Sofia 1978; James & Kahn 1970, 1971). Here $H_{\rm T} := -(\mathrm{d}r)/(\mathrm{d}\ln T)$ is the temperature scale-height and $H_{\rm j} := (\mathrm{d}r)/(\mathrm{d}\ln j)$, the scale-height of the angular momentum distribution. The GSF instability has the same μ-dependence as Eddington-Sweet circulation (Endal & Sofia 1978) and therefore the resulting circulation velocity is computed in the same way, taking the stabilizing effect of the μ-gradient into account:

$$v_{\rm GSF} := \max\{|v_{\rm g}| - |v_\mu|, 0\} \ . \tag{43}$$

Again, the diffusion coefficient is determined from the circulation velocity, $v_{\rm GSF}$, and the minimum of the circulation velocity scale height, $H_{\rm v,GSF}$, and the extent, $d_{\rm inst}$, of the instability:

$$D_{\rm GSF} := \min\{d_{\rm inst}, H_{\rm v,GSF}\} v_{\rm GSF} \ , \tag{44}$$

where we define in the same way as above

$$H_{\rm v,GSF} := \left| \frac{\mathrm{d}r}{\mathrm{d}\ln v_{\rm GSF}} \right| . \tag{45}$$

Fig. 4 compares the parameter space in which the GSF and the Eddington-Sweet instability operate. For small angular velocity gradients the Eddington-Sweet circulation dominates, while the GSF instability becomes more important as the differential rotation increases. Note that for strong differential rotation the shear instability also occurs (cf. Fig. 1)

2.4. Other instabilities

The five instabilities discussed in the previous section are not a complete list of all rotationally induced instabilities for massive stellar evolution. However, they appear to be the most relevant ones, or at least the best understood.

For the ABCD-instability (Spruit et al. 1984) and the triply diffusive instability (Knobloch & Spruit 1983), no reliable estimates of efficiency exist. Furthermore, non-axisymmetric instabilities may also exist, but are poorly investigated so far.

Another important issue is the interaction of the different instabilities, and the interaction of rotation and rotationally induced instabilities with the instabilities listed in Sect. 2.2. The interaction of the shear instabilities and the Eddington-Sweet circulation has been investigated by, e.g., Chaboyer & Zahn (1992); Zahn (1992); Urpin et al. (1996); Meynet & Maeder (1997); Maeder (1997a); Talon & Zahn (1997); Talon et al. (1997); Maeder & Zahn (1998), and semiconvection has recently also been included by Maeder (1997a) and Maeder & Zahn (1998). However, the effects of the interactions are not large and therefore not taken into account in the present work.

Perhapes most importantly, we have neglected magnetic fields. Magnetic fields might transport angular momentum by torques ($\sim r^3 B_r B_\phi$; Spruit 1997), or cause instabilities by magnetic buoyancy resulting from the winding up of magnetic field lines by differential rotation. This could be effective even if the initial field strength is small (Spruit 1997; Spruit & Phinney 1998). Unfortunately, little is known about either the strength of the initial field or the efficiency of instabilities in amplifying the magnetic field. The Velikhov-Chandrasekhar instability depends only on the presence of magnetic fields, not on their strength, but it is efficiently suppressed by μ-gradients (Acheson 1978; Spruit 1997). Detailed studies of the action of magnetic fields inside stars must be left to future investigations.

2.5. Angular momentum transport

Following Endal & Sofia (1978) and Pinsonneault et al. (1989), we formulate the transport of angular momentum as a diffusive process,

$$\left(\frac{\partial\omega}{\partial t}\right)_m = \frac{1}{i}\left(\frac{\partial}{\partial m}\right)_t\left[(4\pi r^2\rho)^2 i\nu\left(\frac{\partial\omega}{\partial m}\right)_t\right] - \frac{2\omega}{r}\left(\frac{\partial r}{\partial t}\right)_m\left(\frac{1}{2}\frac{\mathrm{d}\ln i}{\mathrm{d}\ln r}\right) \tag{46}$$

(Endal & Sofia 1978), where ν is the turbulent viscosity and i, the specific angular momentum of a shell at mass coordinate m. For a spherical shell of constant density, inner radius r_i and outer radius r_o, the specific moment of inertia, i, is given by $i = 0.4\left({r_\mathrm{o}}^5 - {r_\mathrm{i}}^5\right)/\left({r_\mathrm{o}}^3 + {r_\mathrm{i}}^3\right)$; for a thin shell of radius r this simplifies to $i = 2/3\,r^2$. The last term in Eq. (46), an advection term, accounts for contraction or expansion of the layers at constant mass coordinate. The factor in the last bracket on the right hand side vanishes if the gyration constant $k := i/r^2$ does not depend on r.

Eq. (46) is essentially a diffusion equation for ω along the "moment of inertia coordinate",

$$I(m) := \int_0^m i(m')\,\mathrm{d}m' \ , \tag{47}$$

defined analogously to the mass coordinate (e.g., Kippenhahn & Weigert 1991). This equation conserves angular momentum and leads to rigid rotation in a region of extent ℓ whenever the diffusion time-scale, $\tau_\mathrm{D} := \ell^2/\nu$, is short in comparison to structural changes of the star.

At the inner and outer boundary, reflecting conditions similar to those given in Eq. (7) for the compositional mixing are used. At the surface of the star, the angular momentum contained in the layers which are lost due to stellar winds is removed from the star (Sect. 2.7).

The turbulent viscosity, ν, is determined as the sum of the convective and semiconvective diffusion coefficients, and those from rotationally induced instabilities (Endal & Sofia 1978; Sect. 3). In contrast to Endal & Sofia (1978) and Pinsonneault et al. (1989), in the present work the transport equation for angular momentum is solved for the entire star as a whole.

Since the evolutionary time-scale of the star is in most cases much longer than the convective time-scale, Eq. (46) results in rigid rotation in those regions. Unlike composition, which can show significant gradients even inside convective regions due to burning (e.g., during central silicon burning), angular momentum is locally conserved, and therefore convective regions can more easily reach rigid rotation than chemical homogeneity during hydrostatic burning phases. This, however, does not hold if the respective layers are contracting or expanding rapidly.

The approximation that convection leads to rigid rotation rather than constant specific angular momentum seems to be justified, at least if the rotational period is long in comparison to the convective time scale, and it may also hold for more rapid rotation if convective blobs can be assumed to scatter elastically (Kumar et al. 1995). The latitudinally averaged rotation rate of the solar convection zone deviates from solid body rotation by less than 5 % (e.g., Antia et al. 1997).

2.6. Enhanced mass loss due to rotation

Mass loss from the stellar surface ("stellar winds") significantly affects the evolution of massive stars (Chiosi & Maeder 1986). In the present work, the empirical mass loss rate of Nieuwenhuijzen & de Jager (1990) is used. For Wolf-Rayet stars, the prescription of Langer (1989) is applied. The uncertainties in these mass loss rates are considerable due to the uncertainties in the observational data and their interpretation.

These mass loss rates are further modified to account for the effect of stellar rotation according to Friend & Abbott (1986)

$$\dot{M}(\omega) := \dot{M}(\omega = 0) \times \left(\frac{1}{1-\Omega}\right)^{\xi} , \qquad \xi \approx 0.43 , \tag{48}$$

where

$$\Omega := \frac{v}{v_{\rm crit}} , \tag{49}$$

is the ratio of the equatorial surface rotation rate to the critical rotation rate defined by

$${v_{\rm crit}}^2 := \frac{Gm}{r}(1-\Gamma) . \tag{50}$$

The Eddington factor,

$$\Gamma := \frac{\kappa L}{4\pi c G m} , \tag{51}$$

is evaluated only in the radiative part of the optical depth range $\tau \in [2/3, 100]$ (Lamers 1993; Langer 1997), where $\tau(r) = \int_r^\infty \kappa\rho\,\mathrm{d}r$ has the usual definition.

The quantitative result for the Ω-dependence of the mass loss rate obtained by Friend & Abbott (1986) was questioned by Owocki et al. (1996), who performed hydrodynamic simulations of the winds of rotating hot stars including the effect of non-radial radiation forces and gravity-darkening in the approximation of von Zeipel (1924a,b). However, the only crucial ingredient for the model calculations, which is confirmed by Owocki & Gayley (1997), is the fact that the mass loss rate increases strongly as the star approaches the Ω-limit, so that the star cannot exceed critical rotation, but rather loses more mass and angular momentum (Langer 1998).

2.7. Angular momentum loss

The loss of angular momentum from the surface due to stellar winds is approximated by removing of the angular momentum along with the surface layer, i.e.,

$$\dot{J} = \dot{M} j_{\rm surf} , \tag{52}$$

where $j_{\rm surf}$ is the latitudinally averaged specific angular momentum at the surface of the star when the mass loss is assumed independent of latitude.

3. Calibration of the mixing efficiencies

The diffusion coefficients used in this work are subject to considerable uncertainties, as they result from order-of-magnitude estimates of some of the relevant time- and length-scales. Therefore, efficiency factors of order unity are introduced, in order to calibrate the diffusion coefficients with observational data. This is similar to the treatment of Pinsonneault et al. (1989).

The first adjustable parameter is the ratio of the turbulent viscosity to the diffusion coefficient, $f_{\rm c} := D/\nu$. The contribution of the rotationally induced instabilities to the diffusion coefficient is assumed to be reduced by the factor $f_{\rm c}$, while their full value enters the turbulent viscosity,

$$D = D_{\rm conv} + D_{\rm sem} + f_{\rm c}(D_{\rm DSI} + D_{\rm SHI} + D_{\rm SSI} + D_{\rm ES} + D_{\rm GSF}) , \tag{53}$$

$$\nu = D_{\rm conv} + D_{\rm sem} + D_{\rm DSI} + D_{\rm SHI} + D_{\rm SSI} + D_{\rm ES} + D_{\rm GSF} . \tag{54}$$

The second parameter, $f_\mu \in [0,1]$, describes the sensitivity of the rotationally induced mixing to μ-gradients, i.e., ∇_μ is replaced by $f_\mu \nabla_\mu$.

In order to reproduce the surface ^{7}Li abundance in the sun, Pinsonneault et al. (1989) introduced the factor $f_{\rm c} \in [0,1]$. They found a value of $f_{\rm c} = 0.046$ for their best fit. From theoretical work Chaboyer & Zahn (1992) found a similar value, $f_{\rm c} = 1/30$, for the combined action of shear and meridional circulation. This is the value chosen for most of the models presented in this work (cf. Table 3).

The best observational probe of rotationally induced mixing in stars is the evolution of the surface composition during central hydrogen burning.

While lithium and boron are depleted early during this phase (Venn et al. 1996; Fliegner et al. 1996), since they are destroyed at relatively low temperatures, ^{14}N, is only produced at higher temperature, i.e., much deeper inside the star. Therefore, an increase of nitrogen at the surface should be accompanied by an decrease of carbon (^{12}C) or, in the case of even deeper mixing, oxygen (^{16}O), which is destroyed at even higher temperatures.

An enrichment of nitrogen of order $2\ldots3$ is observed for evolved stars of about 10 to $20\,\mathrm{M}_\odot$ (Gies & Lambert 1992; Herrero 1994; Vrancken et al. 1998). Since observations can only give the projected rotation rate and are also restricted to low projected rotational velocities ((Gies & Lambert 1992; Vrancken et al. 1998)), only a qualitative comparison with our models is possible.

The processing of carbon to nitrogen which occurs at core hydrogen ignition does not introduce large μ-gradients. Therefore, the occurrence of a surface nitrogen enrichment and carbon depletion is rather insensitive to f_μ. In contrast, any enrichment of helium in O stars (Herrero et al. 1992, 1998) strongly restricts f_μ. Unfortunately, helium abundances are hard to measure and correspondingly uncertain (Herrero 1994).

For purposes of calibration, we computed evolutionary sequences for solar metallicity stars in the mass range $4\,\mathrm{M}_\odot$ to $60\,\mathrm{M}_\odot$ through core hydrogen burning, adopting a typical zero-age main sequence rotational velocity of $\sim 200\,\mathrm{km\,s^{-1}}$ (Slettebak 1970; Fukuda 1982; Lang 1991; Halbedel 1996; Penny 1996). Fig. 5 shows the surface values of helium, carbon, nitrogen, and oxygen at core hydrogen exhaustion as function of the initial stellar mass for various combinations of f_μ and f_c.

A value of $f_\mu = 0.05$ reproduces an enhancement of nitrogen by a factor of 2 to 3 in the mass range $10\,\mathrm{M}_\odot$ to $20\,\mathrm{M}_\odot$, and results in a surface helium mass fraction of $\sim 40\,\%$ for the $60\,\mathrm{M}_\odot$ star, while the enrichment remains quite small for stars below $20\,\mathrm{M}_\odot$. For $f_\mu = 0.01$, nitrogen and helium are clearly enriched too much for stars below $30\,\mathrm{M}_\odot$. On the other hand, the nitrogen enrichment might be too low for values of $f_\mu \geq 0.1$. Certainly, for $f_\mu = 0.25$ and $f_\mu = 1.0$ the nitrogen abundance for the most massive stars ($30\,\mathrm{M}_\odot \ldots 60\,\mathrm{M}_\odot$) is inconsistent with the observations. The same is true for the helium abundances.

In summary, $f_\mu = 0.05$ seems to be the best value (provided $f_\mathrm{c} = 1/30$; see above). This set of parameters is used in the present work for the models whose name ends with "B" (Table 3). The consequences of a variation of f_c (for fixed $f_\mu = 0.05$) is shown in Fig. 6 for a $12\,\mathrm{M}_\odot$ star. For small values of f_c the nitrogen abundance is too low, while for large values, helium becomes quite high.

As discussed above, too much surface enrichment occurs with $f_\mathrm{c} = 1/30$ for small values of f_μ ($\lesssim 0.01$). Nevertheless, it is interesting to investigate the case where μ-gradients are completely neglected, since the calibration of f_c and f_μ is not unambiguous, and different combinations might result in similar surface enrichments. The surface abundance, however, are the only clear observational constraint, while the degree of internal mixing is not directly observable. Therefore, a second parameter set of $f_\mathrm{c} = 0.01$ and $f_\mu = 0$ is also used. The resulting surface abundances (displayed as thick grey line in Fig. 5) show quite similar enrichments. Models with this choice of f_c and f_μ do *not* carry a "B" at the end of their name (Table 3). A value of $f_\mathrm{c} = 0.01$ for $f_\mu = 0$ is also supported by calibrations of the lithium, beryllium and boron surface abundance for the sun by Fliegner (1993).

4. Numerical solution

Two different numerical codes were used here to follow the stellar evolution. We now briefly describe each.

4.1. STERN

The STERN code is a pseudo-Lagrangian, implicit hydrodynamic code (Langer et al. 1988), based on the "Göttinger stellar evolution code". For numerical solution, relative mass coordinate $q := m/M$ is used instead of the the mass coordinate m, which allows to reserve the distribution of computational grid in the presence of mass loss.

The equation of state includes radiation, ionization, relativistic electron degeneracy, and electron-positron pairs. Ions are treated as a Boltzmann gas (El Eid & Langer 1986).

The chemical evolution due to thermonuclear burning is traced by 35 isotopes: n, $^{1,2}H$, $^{3,4}He$, $^{6,7}Li$, $^{7,9}Be$, $^{8,10,11}B$, $^{11,12,13}C$, $^{12,14,15}N$, $^{16,17,18}O$, ^{19}F, $^{20,21,22}Ne$, ^{23}Na, $^{24,25,26}Mg$, $^{26,27}Al$, $^{28,29,30}Si$, and ^{56}Fe. Except for ^{19}F, ^{26}Al, and ^{56}Fe, reactions between them are solved in a 32 isotope network. These reaction rates are also used to determine the nuclear energy generation rate. The Ne/Na and Mg/Al hydrogen-burning cycles are solved separately using a 13 isotope network including ^{1}H, ^{18}O, ^{19}F, ^{20,21,22}Ne, ^{23}Na, ^{24,25,26}Mg, ^{26,27}Al, ^{28}Si, and ^{16}O (Braun 1997). The neutrino losses are determined according to Munakata et al. (1985).

The reaction networks are solved separately for each zone between the individual stellar structure integration time-steps. This allows for subcycling of the reaction network with fine time-steps wherever needed.

4.2. KEPLER

In the KEPLER code (Weaver et al. 1978, 1984; Woosley & Weaver 1988) the equation of state includes a crude treatment of Coulomb corrections, beyond what is used in STERN (Weaver et al. 1978). A 19-isotope network is employed through oxygen burning, including the elements ^{1}H, ^{3}He, ^{4}He, ^{12}C, ^{14}N, ^{16}O, ^{20}Ne, ^{24}Mg, ^{28}Si, ^{32}S, ^{36}Ar, ^{40}Ca, ^{44}Ti, ^{48}Cr, ^{52}Fe, ^{54}Fe, ^{56}Ni and neutrons and protons from photodisintegration. Silicon burning is followed using a quasi-equilibrium network of 137 isotopes, in which subgroups of elements are treated in nuclear statistical equilibrium while reactions between these subgroups are considered explicitly. Beyond silicon burning full nuclear statistical equilibrium is assumed. A more detailed description of the reaction networks in KEPLER can be found in Weaver et al. (1978). However, an improvement of the treatment of hydrogen burning has been implemented (Appendix A).

For the present work, angular momentum has been added to KEPLER as a new local variable, and rotationally induced mixing processes incorporated according to Sect. 2.3. However, because changes to the structural model calculations on KEPLER would be difficult, the modifications to the momentum balance and the energy transport (Sect. 2.1) applied in STERN are not included into KEPLER. The same opacities (Iglesias & Rogers 1996) used in STERN are also included in KEPLER (an update to previous versions of the code), which allows for more consistency between the two calculations. For temperatures above 10^9 K the opacities used in KEPLER are still chiefly due to electron scattering with corrections due to relativity and degeneracy (Weaver et al. 1978).

As outer boundary conditions a finite (or zero) boundary pressure is often utilized in KEPLER. The radius of the photosphere is determined as the location where an optical depth of 2/3 is reached. This treatment of the outer boundary condition, but also the mass loss, is less accurate than that implemented in STERN (Heger 1998). For this reason, the stellar evolution from the pre-main sequence until a central temperature of $10^9\,$K, i.e., before central neon ignition, is followed by STERN, and the rest of the evolution until core collapse by KEPLER. At this stage of evolution, the total mass lost in its remaining lifetime ($\lesssim$ 100 yr) prior to core collapse is negligible. The stellar envelope, and therefore the outer appearance of the star, hardly changes. However, stellar models followed form the pre-main sequence using KEPLER give results similar to those obtained by STERN.

5. Initial models

The initial model for the calculations presented in this work is that of a fully convective, rigidly rotating (following our assumption that convection does lead to rigid rotation) pre-main sequence star. In the Hertzsprung-Russell (HR) diagram such stars are located on their Hayashi line. These models are constructed from the Lane-Emden equation (e.g., Kippenhahn & Weigert 1991) with a polytropic index of $n = 3/2$. Typically, initial stellar radii around $1\,000\,\mathrm{R}_\odot$ are used. This kind of initial condition is for computational convenience only and is not intended to reproduce the true pre-main sequence evolution (see also Beech & Mitalas 1994; Bernasconi & Maeder 1996).

The influence of rotation on the stellar structure is negligible in the initial models, but it becomes more important when the stars contract towards central hydrogen ignition. On the zero-age main sequence (ZAMS) close-to rigid rotation establishes throughout the star, mainly through the action of Eddington-Sweet circulation (Sect. 2.3.4) and the Goldreich-Schubert-Fricke instability (Sect. 2.3.5). These processes are sufficiently efficient in the early stellar evolution that rigid rotation is established virtually independent of the initial angular momentum distribution assumed. Almost no angular momentum is lost before the star reaches the main sequence.

All models in this work use an approximately solar initial chemical composition with a mass fraction of all elements heavier than helium (“metals”) of $Z = 0.02$. The mass fractions of hydrogen and helium are set to $X = 0.7$ and $Y = 1 - X - Z = 0.28$, respectively. In STERN (Sect. 4.1), the abundance ratios of the isotopes within each of these groups are chosen to have the solar system meteoritic abundance ratios according to Grevesse & Noels (1993) (see Table 1). Calculations performed with the KEPLER code (Sect. 4.2) start on the pre-main sequence with a relative distribution of the metals according to Anders & Grevesse (1989) as given in Table 2.

For the main set of models in this work the initial angular momentum is determined such that the stars reach a rotational velocity of $\sim 200\,\mathrm{km\,s^{-1}}$ on the ZAMS. This is a typical observed value for stars in the mass range $8\,\mathrm{M}_\odot \ldots 25\,\mathrm{M}_\odot$ (Slettebak 1970; Fukuda 1982; Halbedel 1996; Penny 1996; Howarth et al. 1997). It corresponds to $\sim 35\,\%$ of their "critical" rotation speed (Sect. 2.6). Also models with different initial rotation rates are computed, in order to investigate the influence of this parameter on the evolution of massive stars (see Table 3).

6. Central hydrogen burning

6.1. Chemical mixing: the example of $20\,\mathrm{M}_\odot$ stars

In Fig. 7 the internal profiles of the most abundant isotopes in a non-rotating star and two rotating $20\,\mathrm{M}_\odot$ models are compared at core hydrogen exhaustion. Convection causes flat profiles in the innermost few solar masses. Small convective and/or semiconvective regions (similar to Model `D15` in Fig. 17) cause steps in the profile above the convective core.

In the non-rotating case no mixing occurs in the envelope. In contrast, the rotating models mix thermonuclear processed matter into the envelope. If no inhibition of rotationally induced instabilities by μ-gradients is assumed an extended gradient in helium (along with other species) reaches from the upper edge of the convective core up to the surface (Model `E20` in Fig. 7A). Due to the increase of the mean molecular weight in the whole envelope, as a consequence of helium enrichment, the mass of the hydrogen-depleted core of Model `E20` is about $1.5\,\mathrm{M}_\odot$ larger than in the non-rotating case.

The dominant rotationally induced mixing process during central hydrogen burning is Eddington-Sweet circulation. It is fast enough to keep the whole star close to rigid rotation (Sect. 6.2), and thus renders shear instabilities unimportant. The GSF instability remains one to two orders of magnitude less efficient than the Eddington-Sweet circulation. The μ-gradients above the convective core in Model `E20` (see also Fig. 18) are strong enough to suppress the occurrence of extended semiconvective structures. The secular shear instability occurs only in a small layer close to the surface, and never contributes significantly to the mixing.

If μ-gradients *are* taken into account for the rotationally induced instabilities (Model `E20B`; Figs. 7B and 19), the μ-gradient which forms at the upper edge of the convective core is not smoothed out fast enough, but instead almost completely chokes off any mixing between core and envelope quite early during core hydrogen burning. Therefore, below $m = 10\,\mathrm{M}_\odot$ the composition of Model `E20B` remains quite similar to that of Model `D20`. The higher concentration of carbon in Model `E20B`, however, shows the occurrence of *some* mixing early on.

Above the "barrier" due to the μ-gradient (μ-barrier) mixing is efficient (see the small slope of the composition profiles in the envelope of Model `E20B`; Fig. 7B), and stronger than for Model `E20`, since the efficiency for compositional mixing is assumed to be $f_\mathrm{c} = 1/30$ in Model `E20B` instead of $f_\mathrm{c} = 1/100$ for Model `E20`.

The relative contributions of the different rotationally induced mixing processes above the μ-barrier are similar in Models `E20` and `E20B`, except that close to the μ-barrier the GSF instability becomes important in Model `E20B`. Within the μ-barrier, almost all rotationally induced mixing is suppressed and the mixing is dominated by semiconvection. The secular shear instability is inhibited by the μ-gradient.

Strong angular velocity gradients at the boundaries of convective layers cause, in principle, layers where the shear flow can overcome the stabilizing effect of the μ-gradients. However, they are too thin to be resolved in the present calculations.

6.2. Transport of angular momentum

Similar to chemical mixing, the transport of angular momentum depends strongly on the inhibition of rotationally induced mixing by μ-gradients. Fig. 8 compares the internal angular velocity profile of two $15\,\mathrm{M}_\odot$ stars (Models `E15` and `E15B`) which were computed with different values of f_μ (Sect. 3).

In Model `E15`, the difference between surface and core angular velocity remains less than $30\,\%$ during core H-burning. The over-all decrease of the rotation rate by a factor of ~ 3 is caused by two effects: mass loss from the surface, which carries away $\sim 40\,\%$

of the initial angular momentum, and the expansion of the stellar envelope, which increases the total moment of inertia by a factor of ~ 2. At the same time, the stellar core contracts. The persistence of almost rigid rotation during core hydrogen burning implies transport of angular momentum from the core to the envelope. This is confirmed by Fig. 8C which shows a decrease of the core specific angular momentum with time (see also Fig. 8E). Because of its small radial extent, the core contains only a small fraction of the total angular momentum of the star (Figs. 8E and F). For higher mass loss rates, i.e., for more massive stars, the spin-down (decrease of ω) is dominated by the mass loss, while at lower mass it is dominated by the expansion of the envelope.

Fig. 8B shows that the inhibition of rotational mixing leads to differential rotation during core hydrogen burning. The ratio of the core to envelope angular velocity in Model `E15B` becomes ~ 4 at core hydrogen exhaustion. The envelope rotates slightly faster than in Model `E15` since the star loses only 20 % of the initial total angular momentum, i.e., about half as much as Model `E15`. This is due to the lower luminosity of Model `E15B` during core hydrogen burning — due to less efficient chemical mixing (Sect. 6.1) — and consequently about 60 % less mass loss than in Model `E15`. Figs. 8D and 8F show that in Model `E15B` the core angular momentum is constant throughout core hydrogen burning.

Figs. 8E and F compare the angular momentum distribution of Model `E15` and Model `E15B` at various evolutionary stages using the variable $J(m)/m^{5/3}$, with $J(m) := \int_0^m j(m')\,\mathrm{d}m'$. Since for a rigidly rotating body of constant density, ρ_0, the angular momentum $J(m)$ enclosed by the mass coordinate m is

$$J(m) = \frac{3\omega k}{5}\left(\frac{3}{4\pi\rho_0}\right)^{2/3} m^{5/3} \propto m^{5/3} \qquad (55)$$

the curves in Figs. 8E and F are more or less flat. The evolution of $J(m)$ illustrates the transport of angular momentum throughout stellar evolution. $J(m)$ drops when angular momentum is transported through the mass shell m. If no transport angular momentum through the mass shell m occurs, $J(m)$, and also $J(m)/m^{5/3}$, remain constant. Furthermore, following a line of constant J from one evolutionary stage to a subsequent one shows to what mass coordinate angular momentum has been transported in the star during the time between the two evolutionary stages. We will refer more to Figs. 8E and F in the discussion of the angular momentum transport during the later evolutionary phases.

6.3. The influence of the initial rotation rate

Fig. 9 show the evolution of angular velocity and specific angular momentum in Models `G15B` and `F15B`, which both contain the inhibition of rotational mixing due to μ-gradients. The latter model initially has three times more angular momentum than the first.

While this difference of a factor of three in the rotation rate is conserved in the envelope throughout core hydrogen burning, it becomes much smaller in the cores. The faster rotation of Model `F15B` sustains the transport of angular momentum out of the core for a longer time than in Model `G15B`, where the core angular momentum is almost completely conserved (Fig. 9). That is, the angular momentum is less efficiently trapped in the fast rotating Model `F15B` than in the Models `G15B` and `E15B` (Figs. 8 and 9). This feedback process leads to a convergence of the core rotation rates. We note already here that this convergence persists during the later burning stages and leads to very similar iron core angular momenta for a wide range of initial rotation rates (cf. Sect. 10 below).

The stronger core angular momentum depletion in faster rotating models occurs simultaneously with rotationally induced mixing across the μ-barrier: The masses of the convective cores at the end of central hydrogen burning are $2.4\,\mathrm{M}_\odot$, $2.5\,\mathrm{M}_\odot$, $2.6\,\mathrm{M}_\odot$, and $2.8\,\mathrm{M}_\odot$ for Models `D15`, `G15B`, `E15B`, and `F15B`, respectively. However, Model `E15`, where the μ-barrier was assumed to be inefficient, has a core of about $3.5\,\mathrm{M}_\odot$. Thus, even for very rapid rotation the assumption of μ-barriers inhibiting rotational mixing strongly restricts the core growth due to rotation. (see also Figs. 17, 18, and 19).

7. Central helium burning

After core hydrogen exhaustion, the models become red supergiants (except for Model `H12B` which first burns helium as a as a blue supergiant for some time) and their extended hydrogen-rich envelopes become convective. The pulsational properties of these envelopes have been discussed by Heger et al. (1997) and the evolution of the surface rotation rates, especially during blue loops, by Heger & Langer (1998). In the following, we investigate the evolution of the cores, using the $15\,\mathrm{M}_\odot$ models as example.

The importance of rotation in the post main sequence evolution can be estimated from Table 4, which compares the Eddington-Sweet time-scale

$$\tau_{\rm ES} \sim \tau_{\rm KH} \left(\frac{\omega_{\rm Kep}}{\omega}\right)^2 , \qquad \omega_{\rm Kep} := \sqrt{Gm/r^3} \, . \quad (56)$$

(Zahn 1992) in the cores of our Models E15 and E15B during the various burning stages with the respective nuclear time scales. For the amount of differential rotation in our models, the characteristic time-scale for mixing due to the GSF instability (Sect. 2.3.5) is comparable to the Eddington-Sweet time-scale.

The core hydrogen burning phase is the only one where mixing and nuclear time scale are comparable. During core helium burning, the mixing time scale is one or two orders of magnitude smaller than the nuclear time-scale, which may still allow for some effects of rotational mixing. The later phases are too short to allow for any rotationally induced mixing in the cores; note however, that at the core boundaries some effects of rotational mixing may still be possible in case of strong gradients in the angular velocity (cf. Sect. 9.1 below).

An energetic limit to the amount of mixing due soley to shear instabilities can be obtained by comparing the rotational energy of the core with the potential energy required to lift processed matter from the upper edge of the convective core to the hydrogen-burning shell source (Heger 1998). For a typical value of $\omega/\omega_{\rm Kep} = 0.05$ and a difference in the mean molecular weight of fully ionized carbon relative to helium of ~ 0.3 (oxygen would be even heavier), an enrichment of carbon by at most $\lesssim 0.5\,\%$ is possible. This assumes the carbon to be homogeneously distributed throughout the radiative layer and that all the rotational energy of the core is used to supply the buoyancy energy. Note that this limit does not apply to instabilities which tap the energy flux in the star like the Eddington-Sweet circulation.

7.1. Chemical mixing

In a non-rotating star using the Ledoux criterion for convection (Sect. 2.2.2) prevents the growth of the convective helium core that would occur if the Schwarzschild criterion were assumed. Instead, several convective regions, separated by semiconvective layers, form above the convective core (Figs. 10C and 17). In the rotating models with $f_\mu = 0.05$ (e.g., Model E15B in Figs. 10B and 19) the shear across the semiconvective layers is not strong enough to overcome the stabilizing μ-gradient, even for the fast rotating Model F15B.

If rotationally induced mixing is assumed to be insensitive to μ-gradients (i.e., $f_\mu = 0$; Model E15 in Figs. 10A and 18) the dynamical shear instability operates in the semiconvective regions and dissolves them, similar to the case of Schwarzschild convection. In this case, the rotational mixing leads to considerably more massive helium cores. The resulting higher burning temperatures in the cores lead to lower central carbon-to-oxygen ratios at core helium exhaustion.

An interesting issue is the mixing (and angular momentum transport) in the radiative helium layer between the convective core and the hydrogen-burning shell. If the products of helium burning could be mixed upward into the hydrogen-burning shell, *primary* production of ^{14}N could occur. If hydrogen were transported down into the helium-burning center, a much stronger than normal s-process could result and build up more heavy or neutron-rich elements. On the other hand, strong instabilities in this region could also lead to a significant slowing-down of the core.

The dominant mixing process present in this layer is Eddington-Sweet circulation, with some contribution from the GSF instability. During the early stages of core helium burning of models with $f_\mu = 0$ (e.g., Model E15), the secular shear instability dominates slightly over the Eddington-Sweet circulation at the upper edge of the helium core. Towards central helium exhaustion, the mixing is dominated by the GSF instability. In the case of $f_\mu = 0.05$, the secular shear instability is suppressed by μ-gradients.

Fig. 10B illustrates that some mixing occurs during core helium burning: A gradient in ^{12}C and ^{16}O extends from the convective core up to the edge of the helium core. In this model, the increase in ^{12}C or ^{16}O is not sufficient to result in any significant primary nitrogen production in the hydrogen burning shell. Even though this effect is not notably more pronounced in the initially faster rotating Model F15B — due to the convergence of the core rotation rates; cf. Sect. 6.3 — or for the different initial masses investigated here, such a primary nitrogen production appears possible in more favorable conditions, e.g., for higher mixing efficiencies or at lower metallicity.

In Model E15 (Fig. 10A) the rotation of the helium core is slower, and the ^{12}C and ^{16}O gradients are much steeper, leveling off to the CNO equilibrium values a few tenths of a solar mass above the convective core. In the non-rotating Model D15 (Fig. 10C), no enrichment of ^{12}C and ^{16}O appears at all above the outermost semiconvective layer of the convective core.

Even though the strong entropy gradient at the location of the hydrogen-burning shell suppresses rotational mixing between the helium core and the hydrogen burning shell, some mixing occurs due to the large angular velocity gradient. This can be seen in Fig. 19: The tail of the energy generation rate at the lower bound of the hydrogen-burning shell source in Model E15B penetrates into the helium core, i.e., some hydrogen is mixed downward. Since the protons burn quite fast as they are mixed deeper inside the helium core, they cannot reach the central convective region. However, some protons may survive and get mixed into the convective helium shell later on (Sect. 9.1). In Model E15 (Fig. 18), where the core is rotating slower, and also in the non-rotating Model D15 (Fig. 17), this feature is not found.

7.2. Transport of angular momentum

After core hydrogen exhaustion, the stars undergo a phase of major restructuring as the core contracts and the envelope expands. This leads to a spin-up of the core (Figs. 8A and B, 9A and B) and a spin-down of the envelope. At the same time, the convective envelope grows in mass and its bottom approaches the helium core. A steep rise in the specific angular momentum occurs at the bottom of the rigidly rotating envelope that persists throughout core helium burning and beyond (Figs. 8C and D, 9C and D). The entire helium core stays close to rigid rotation during central helium burning (Figs. 8A and B, 9A and B).

Up to core helium exhaustion, the specific angular momentum of the helium core drops appreciably with time (Figs. 8 and 9). Three processes contribute to this effect. First, angular momentum is removed from the core during the star's restructuring phase between core hydrogen depletion and helium ignition. Second, the core grows in mass due to hydrogen shell burning and engulfs regions of lower specific angular momentum (Figs. 8C and D). The reasons for the low specific angular momentum above the core are secular shear instabilities, the *first dredge-up*, and short-lived convective regions which temporarily extend down to mass coordinates smaller than the final helium core mass. The regions of outwards decreasing specific angular momentum are not Solberg-Høiland unstable due to strong stabilizing entropy and composition gradients. Third, some angular momentum is transported from the helium core into the envelope through the hydrogen-burning shell. The models of the "B" series lose less angular momentum during the restructuring phase because of the inhibiting effect of the μ-gradients, but more during central helium burning, due to their considerably faster rotation.

The relative loss of angular momentum in Models G15B, E15B, and F15B during helium burning increases with the initial amount of angular momentum left at the end of central hydrogen burning. Consequently all three models end up with very similar core angular momenta and rotation rates (Fig. 9), about three times that of Model E15 (Fig. 8).

8. Comparison with previous work

In contrast to Kippenhahn et al. (1970), who investigated rapidly rotating $9\,M_{\odot}$ stars ($v \gtrsim 400\,\mathrm{km\,s^{-1}}$), our models do not become secularly unstable at the end of central helium burning, since, according to our assumptions, μ-barriers are less efficient in suppressing angular momentum transport compared to Kippenhahn et al. (1970).

Endal & Sofia (1978) followed the evolution of $7\,M_{\odot}$ and $10\,M_{\odot}$ stars with a ZAMS rotational velocity of $\sim 200\,\mathrm{km\,s^{-1}}$ using essentially the same method as in the present work, except for some improvements in the input physics of the individual processes applied here (Sect. 2.2 and Endal & Sofia 1978). They used the Schwarzschild criterion for convection, however, and did not include mass loss. In their work, the μ-barrier above the convective hydrogen-burning core suppressed mixing and transport of angular momentum almost completely. Therefore, their stellar cores lose very little angular momentum during central hydrogen burning. Although we use $f_{\mu} < 1$ and the inhibiting effect of the μ-gradients is smaller, a similar μ-barrier forms during central hydrogen burning. However, we obtain some mixing between the core and the envelope early during core hydrogen burning, some angular momentum loss from the core to the envelope, and in most cases some enrichment of the surface with H-burning products. In an earlier work, Endal & Sofia (1976) disregarded rotationally induced angular momentum transport, but imposed various rotation laws. In this case an even more extreme result was obtained: all models reached critical rotation before carbon ignition.

Eryurt et al. (1994) considered turbulent diffusion according to Zahn (1983) in their computation of a rotating $20\,\mathrm{M}_\odot$ stars with a metallicity of $Z = 0.008$. They found a surprisingly large surface $^{14}\mathrm{N}$ enrichment at the end of core hydrogen burning of more than 2 % by mass. Since the CNO cycle conserves the total mass of the CNO isotopes, this result appears implausible and cannot be reproduced in the present work.

Meynet & Maeder (1997) used a prescription for the Eddington-Sweet circulation according to Zahn (1992), and a modified Richardson criterion to account for thermal effects (Maeder 1995; Maeder & Meynet 1996). They computed the hydrogen-burning evolution of stars from $9\,\mathrm{M}_\odot$ to $60\,\mathrm{M}_\odot$ and found a strong inhibiting effect of the μ-gradients on the rotational mixing, which resulted in stronger differential rotation at core hydrogen exhaustion than found in our models of the "B" series. Their models did not show any surface enrichment of helium.

These models were superseded by those of Meynet (1997), who computed the main sequence evolution of $20\,\mathrm{M}_\odot$ and $40\,\mathrm{M}_\odot$ stars, using improved physics of rotationally induced mixing as discussed by Meynet & Maeder (1997), and Maeder (1997b). The inhibiting effect of μ-gradients on shear mixing and Eddington-Sweet circulation was strongly reduced in the new formulation. Meynet's rotating $20\,\mathrm{M}_\odot$ model showed a larger envelope helium enrichment than a comparable models of Model E20, and a similar mass of the hydrogen-depleted core. The physics used in Meynet (1997) has been revised again by Maeder & Zahn (1998) for a more consistent treatment of μ-gradients. Models with this prescription are not yet available.

Talon et al. (1997) followed the main sequence evolution of $9\,\mathrm{M}_\odot$ stars with ZAMS rotation rates of $100\,\mathrm{km\,s^{-1}}$ and $300\,\mathrm{km\,s^{-1}}$ until end of central hydrogen burning, using the prescription for the Eddington-Sweet circulation by Zahn (1992). The helium enrichment in the envelope showed a smooth profile, similar to our Models E08 and E10. At core hydrogen exhaustion, their models showed steep composition gradients close to the stellar surface. This may have resulted from the low mass loss assumed in their calculation in combination with inefficient mixing close to the surface. With a slightly larger mass loss rate, their rapidly rotating model would have a much stronger surface enrichment. Due to the downward advection of angular momentum by meridional circulation in the theory of Zahn (1992), Talon et al. (1997) found a somewhat stronger envelope differential rotation compared to our Models E08 and E10, but a comparable one to, e.g., Model E12B. We conclude that this downward advection is not a strong effect, which may justify its neglect in the present work.

Summarizing, the prescription for rotationally induced mixing used in the model of Kippenhahn et al. (1970) corresponds roughly to $f_\mu = f_\mathrm{c} = \infty$ in terms of the present formulation. Endal & Sofia (1978) used about $f_\mu = f_\mathrm{c} = 1$. Neither work obtained any surface enrichment during core hydrogen burning due to the strong inhibiting effect of μ-gradients (Meynet & Maeder 1997). The recent picture of interacting Eddington-Sweet circulation, anisotropic turbulence and shear instabilities (Chaboyer & Zahn 1992; Maeder & Zahn 1998) has been continuously improved in the last years (e.g., Urpin et al. 1996; Maeder 1997b; Talon & Zahn 1997; Talon et al. 1997). The most recent work in this series, Maeder & Zahn (1998), includes an improved treatment of compositional gradients, but this type of description for rotationally induced mixing is complex, computationally expensive, and has not yet been successfully tested for post-hydrogen burning stars. However, the results obtained in earlier work (Talon et al. 1997; Meynet 1997) for massive main sequence stars are not significantly different from those of the present work.

9. Late evolution until core collapse

After core helium exhaustion, the carbon-oxygen core (CO core) contracts and subsequently phases of carbon, neon, oxygen, and silicon central convective and shell burning follow inside this core.

Table 5 gives some key parameters of the final models: the final mass of the star, the masses of the helium, CO, and iron cores, and the angular momenta contained in theses cores. For the iron core additionally the average specific angular momentum is given. Models D10, D12, E08, G12B, E12B, and F12B develop degenerate neon-oxygen cores and central neon burning starts off-center. Due to the computational difficulties (and expense) these models were not followed until core collapse, but stopped during neon or oxygen shell burning or even before neon ignition. In Model D10 even carbon burning ignites off-center. Models D10 and E08 experience a dredge-up of almost the entire helium shell by the convective envelope. Therefore the final helium core is small and has little angular momentum. The remaining helium shell above the CO core at the point where the calculation is ended is only a few hundreths of a solar mass. The masses of the helium cores before the dredge-up are 2.25 and $2.1\,M_\odot$, respectively. Model E25 loses its hydrogen-rich envelope during central helium burning and becomes a Wolf-Rayet star. Strong Wolf-Rayet mass loss sets in and further decreases the mass of the star. It ends up with only $5.45\,M_\odot$ at the time of core collapse and very little angular momentum.

Note that in Table 5 the masses of some of the helium cores in the non-rotating models are apparently larger than those of the slowly rotating models of the "B" series. This is an artifact due to the criterion used to measure the mass of the helium core. We define the helium core by the mass coordinate at which the hydrogen mass fraction drops below 10^{-3}. In the rotating models of the "B" series, the hydrogen gradient at the top of the helium core is significantly shallower. If instead a hydrogen mass fraction of 10^{-2} is chosen, the helium core masses are similar or even larger for the rotating models. Note that the size of the CO core is defined in a similar way: by the mass coordinate at which the helium mass fraction drops below 10^{-3}.

9.1. Chemical mixing in the helium shell

After core helium exhaustion, the CO core contracts and the burning of helium continues in a shell. At the same time, the outer layers of the helium-rich shell cool down and the hydrogen shell source goes out. Since this implies a reduced entropy barrier, rotationally induced mixing through the hydrogen-helium interface can now operate more efficiently. The protons which are mixed downward into the helium shell do not burn immediately. When later the helium-burning driven convective shell extends upwards, it dredges these protons down into the hot, helium-burning layers (see Fig. 19). This mechanism can open new channels of nucleosynthesis. This will be investigated in more detail in forthcoming papers (see Langer et al. 1999 for a first report).

9.2. Chemical mixing inside the CO core

During the final remaining stellar burning phases, rotational mixing inside the CO core is unimportant. The strongest instabilities are again the Eddington-Sweet circulation and the GSF instabilities, at about same order of magnitude. From Table 4 it can be seen that their time scale is too long in order to be significant.

Also, the mixing of *traces* of material into regions of neighboring burning phase is not expected to introduce qualitatively new nucleosynthesis channels, since all abundant nuclear species in one burning phase are anyway present in the neighboring one (e.g., mixing traces of oxygen into neon burning is not exciting).

In the fast rotating cores of the models of the "B" series, secular shear instabilities arise above several of the central and shell convection zones for a limited time, but they do not become efficient enough to cause any noticeable mixing.

9.3. Transport of angular momentum

As for the chemical mixing, rotational mixing cannot effectively remove angular momentum from the core during the late burning stages. In particular, transport is too inefficient to keep the CO core in rigid rotation. Strong differential rotation occurs (Figs. 8A and B, 9A and B). At this time, the only instability capable of enforcing rigid rotation is convection. Since the radii of the lower boundaries of the major convection zones of carbon, oxygen, and silicon burning are much smaller than that of their upper edges, large differences in the specific angular momentum exist between the bottom and the top of the convection zone. Thus, angular momentum is mainly carried outwards. The typical signature of such a convection zone is a steep drop of the specific angular momentum at its bottom, accompanied by a large increase at its top (Figs. 8, 9, and 12).

Convection zones that subsequently overlap can transport angular momentum efficiently over scales larger than their individual extent. This is most efficient when the lower boundary of a convective shell overlaps with the upper boundary of a preceding convection zone. For the models investigated in this work, such an overlap occurs rather infrequently (Appendix B). Subsequent shells, which are driven by nuclear burning, tend to form their lower boundary at the upper edge of a preceding shell, where the fuel for their burning is not yet depleted. The most prominent example of this is the sequence of carbon-burning shells (e.g., Fig. 18). Exceptions occur only for some of the late carbon burning shells, and for the oxygen burning shells in Models G15B and E15B.

Convective angular momentum transport does not operate across the boundary of the CO core. These cores retain their angular momentum after core helium exhaustion. Some redistribution, mainly due to convection, occurs inside the cores. For example, Fig. 8E shows that after core helium exhaustion in Model `E15`) no angular momentum is transported through the shells at $m \approx 3.4\,\mathrm{M}_\odot$ and $m \approx 5.1\,\mathrm{M}_\odot$, i.e., the boundaries of the helium and the CO core, respectively.

In models with more rapidly rotating cores, (Models `G15B`, `E15B`, and `F15B`; Figs. 8F, 9E and F), the helium core does lose some angular momentum, even though its upper boundary (at $m \approx 3.7\,\mathrm{M}_\odot$) remains a significant barrier for angular momentum transport as indicated by the spike in Fig. 8F. The loss of angular momentum from the helium core is correlated with the mixing of hydrogen into the helium shell described in Sect. 9.1. No significant angular momentum was transported across the boundary of the CO core in any of the models (Figs. 8E and F, 9E and F).

9.4. Stability to triaxial deformations

As described in Sect. 2.1, the approximations employed in this work are limited to slow rotation in the sense that no triaxial deformation appear. In the KEPLER code, the influence of the centrifugal forces on the structure is completely neglected. However, when models from calculations with STERN, where centrifugal forces *are* included, are continued by KEPLER at a central temperature of $10^9\,\mathrm{K}$, the evolution usually proceeds smoothly, i.e., these forces *are not* important at this late stage of evolution. On the ZAMS, the rotational energy E_{rot} of the star is negligible in comparison to its gravitational binding energy E_{pot} for all models, even for those which are close to critical rotation at their surface ($E_{\mathrm{rot}}/|E_{\mathrm{pot}}| \ll 1\,\%$).

However, in the course of their evolution the stellar models contract and — as outlined in Sect. 9.3 above — the transport of angular momentum out of the core is inhibited or slow, with the consequence of rapidly rotating cores (Figs. 8A and B, 9A and B, and Table 6). For local angular momentum conservation in a shell with given specific angular momentum j, the ratio of angular velocity to Keplerian angular velocity scales as

$$\frac{\omega}{\omega_{\mathrm{Kep}}} = \frac{j}{k\sqrt{Gmr}} \sim r^{-1/2}\,, \qquad k \approx 2/3\,. \qquad (57)$$

The ratio of the specific rotational energy to the gravitational potential is then given by

$$\frac{e_{\mathrm{rot}}}{\phi_{\mathrm{grav}}} = \frac{1}{2}\left(\frac{\omega}{\omega_{\mathrm{Kep}}}\right)^2\,. \qquad (58)$$

This ratio is displayed for several $15\,\mathrm{M}_\odot$ pre-collapse models in Fig. 11.

A uniformly rotating, self-gravitating, incompressible, and inviscid fluid (McLaurin spheroid) becomes secularly unstable to triaxial deformations when the ratio of rotational to gravitational potential energy

$$\frac{E_{\mathrm{rot}}}{E_{\mathrm{pot}}} = \frac{1}{2}\int_0^m \omega^2(m')\,\mathrm{d}m' \bigg/ \int_0^m {\omega_{\mathrm{Kep}}}^2(m')\,\mathrm{d}m' \qquad (59)$$

exceeds ~ 0.1375 (e.g., Ostriker & Bodenheimer 1973; Tassoul 1978). If this ratio exceeds ~ 0.26, the object becomes dynamically unstable to non-axisymmetric instabilities and fission may occur (Ostriker & Tassuol 1969; Ostriker & Bodenheimer 1973). The stars simulated in the present work are well below these limits even at the pre-collapse stages ($E_{\mathrm{rot}}/E_{\mathrm{pot}} \lesssim 30\,\%$ of the critical value) and therefore no triaxial instabilities arise.

10. Angular momentum prior to core collapse

Our model sequences are terminated at the onset of core collapse, defined by the infall velocity inside the iron core exceeding $9{\cdot}10^2\,\mathrm{km\,s^{-1}}$. At this stage of evolution the investigated stars typically have central densities of $\lesssim 1{\cdot}10^{10}\,\mathrm{g\,cm^{-3}}$. From the previous discussions it is clear that the distribution of angular momentum in the star at onset of core collapse strongly reflects its recent convective structure. Fig. 12 shows the distribution of the specific angular momentum at the pre-collapse stage of $15\,\mathrm{M}_\odot$ stars with different initial rotation rates (Models `G15B`, `E15B`, and `F15B`).

These three models show a very similar final angular momentum distribution (cf. also Fig. 13A), due to a similarity entire chemical structure. The reason for this is the convergence of the core rotation rates, i.e. their independence from the initial rotation rates, already during hydrogen and helium burning, as outlined in Sect. 6.3.

In contrast, Model `E15` has much less angular momentum left in the core (see also Table 5). It grows a larger helium and CO core due to the lack of sensitivity to μ-gradients.

The total angular momentum in the final models is dominated by that of the envelope (Table 5). Models

G15B, E15B, and F15B show that for initially faster rotation, a slightly larger helium core results (Table 5) and therefore the stars become more luminous. This in turn causes more mass and angular momentum loss, which can, for the rapid rotators or for more massive stars, decreases the total angular momentum by a larger factor (Figs. 13B and 14B).

At hydrogen ignition, the total and even the mean specific angular momentum of models with a given surface rotational velocity are larger for larger initial masses (Table 5). On the contrary, the final total angular momentum decreases for larger initial mass (Table 5 and Fig. 14). This trend is only interrupted between 12 and $15\,\mathrm{M}_\odot$ since our models with initial masses of $12\,\mathrm{M}_\odot$ or less undergo a blue loop during core helium burning which leads to an additional strong angular momentum loss (Heger & Langer 1998). As in the limit of vanishing mass loss, the angular momentum of our models is conserved, the decrease of the total angular momentum for higher initial masses is solely due to the increase of the mass loss rate for larger initial masses.

The total angular momentum of the helium and CO cores increases with the the initial stellar mass of our models (Table 5). However, this trend is much weaker for the specific angular momentum of the helium cores, the specific angular momenta of the CO cores even decreases a little with increasing initial mass. This illustrates that angular momentum transport from the core into the envelope is stronger for larger cores.

Finally, we find that the specific angular momenta of the iron cores are rather insensitive to the initial mass and rotation rate (Table 5 and Fig. 15), due to the convergence of the core rotation rates discussed in Sect. 6.3. In the models with $f_\mu = 0$, angular momentum transport was efficient and final values of $j_{\mathrm{Fe}} \simeq 6{\cdot}10^{15}\,\mathrm{cm}^2\,\mathrm{s}^{-1}$ are found. The value for Model E25 is significantly lower since its CO core was spun down in a Wolf-Rayet phase. The models with $f_\mu = 0.05$ all end up with $j_{\mathrm{Fe}} \simeq 1.2{\cdot}10^{15}\,\mathrm{cm}^2\,\mathrm{s}^{-1}$.

Note that, unless the iron core that forms after central silicon burning is already large enough to collapse, one or more subsequent phases of silicon shell burning occur until the critical iron core mass is exceeded. The sizes of these shells depend on the details of the preceding evolution. As a result, the iron core mass does not necessarily increase monotonically with initial mass or rotation. For example, the iron core of Model D20 is larger than those of the $20\,\mathrm{M}_\odot$ models of the "B" series.

11. Implications for young pulsars and supernovae

Table 6 shows, for times during the evolution, the specific angular momentum contained in the innermost $1.7\,\mathrm{M}_\odot$ (the mass of the iron core at core collapse) for Model E20. Due to the continuous contraction of the central region of the star, it spins up and gets closer to critical rotation (Eq. 57). If the precollapse value of the specific angular momentum is applied to a neutron star with an assumed radius of 12 km, it would rotate with 90 % of Keplerian rotation (Table 6). Model E20 has the largest iron core mass of all our models (Table 5), and a lower core specific angular momentum than the models computed with $f_\mu = 0.05$. Those models have even much more angular momentum in the collapsing iron core than a neutron star can possibly carry ($\omega/\omega_{\mathrm{Kep}} \propto jm^{-1/2}$). This much angular momentum would certainly be important in the dynamics of core collapse, and it is expected that significant deviations from spherical symmetry will arise (Imshennik 1995; Aksenov et al. 1997; Zwerger & Müller 1997; Rampp et al. 1998).

11.1. Comparison with observed young pulsars

At 90 % of Keplerian angular velocity, the neutron star which might form in the collapse of the iron core of Model E20 would have a rotation period of 1 ms (Table 6). In Table 7 the periods of the four known young neutron stars associated with supernova remnants (Mashall et al. 1998) are given along with their specific angular momentum (with the same assumption regarding moment of inertia as above). Comparing this to the specific angular momentum in the iron cores found in the pre-collapse models in Table 5, we see that the iron cores of our models have roughly $\sim$ 20 to 100 times more specific angular momentum than found in these neutron stars. Triaxial deformations and gravitational radiation would result — even during the explosion. Still it might be expected that the resulting neutron stars would spin much faster than observed.

However, the observed "young" neutron stars have ages of several hundred years. They might have spun much faster immediately after their formation. In fact, it has been proposed recently that rapidly rotating hot neutron stars are spun down on a time-scale of one year by r-mode oscillations and accompanying emission of gravitational radiation. These oscillations are supposed to cease at spin periods compatible with those observed in the young neutron stars (Lindblom et al. 1998; Owen et al. 1998).

Alternatively, an important angular momentum transport mechanism might be missing in our models (see also Sect. 2.4). Spruit & Phinney (1998) have assumed, without computing detailed models, that the winding up of weak magnetic fields by differential rotation can cause enough Maxwell stress to keep the entire star in uniform rotation until the end of central carbon burning. This scenario approaches the problem of the young neutron star periods from the other side: It implies initial spin periods of $\sim 100\,\mathrm{s}$. Since this is much larger than observed, they employed off-center "kicks" during the supernova explosion to spin them up to the observed rotation rates. This scenario is speculative at present, since neither the evolution of magnetic instabilities in the stellar interior nor the neutron star kicks have been adequately investigated.

11.2. Formation of Kerr black holes?

If the large angular momenta obtained for the iron cores in this work pose a problem for pulsars, they are very favorable for the collapsar model for γ-ray bursts (Woosley 1993). If the cores of the stars would collapse to a black hole, the angular momentum calculated here would be enough to support matter in a stable disk outside (Shapiro & Teukolski 1983; Novikov 1997). This is indicated in Fig. 16, where the distribution of the specific angular momentum at the pre-collapse stage of the two $20\,\mathrm{M}_{\odot}$ Models `E20` and `E20B` is shown. Thin dashes and dash-dotted lines indicate the specific angular momenta of the last stable orbit around a non-rotating and a maximum rotating black hole with a mass equal to the mass coordinate. If the matter in the star has more angular momentum than necessary to get into the last stable orbit, an accretion disc must form, and efficiently transform gravitational binding energy into heat, up to $42.3\,\%$ of the rest mass for a maximum rotating black hole (Shapiro & Teukolski 1983; Novikov 1997). Note that the specific angular momentum displayed in Fig. 16 is the latitudinal average over a shell. Its actual value at the equator is higher than that by $50\,\%$, while it is zero at the pole. Therefore matter might fall in almost freely along the rotation axis, while it hits the centrifugal barrier at the equator. In case a prompt supernova explosion fails and a black hole forms instead of a neutron star, this might be a mechanism for an efficient energy source for supernovae or even a γ-ray burst (Woosley 1993; Popham et al. 1998; MacFadyen & Woosely 1998).

12. Summary and conclusions

We have presented the first complete numerical simulation of the evolution of rotating stars from the ignition of nuclear burning until the supernova stage. Emphasis has been placed on the modification of the evolution induced by rotation. This includes an examination of the transport processes responsible for redistributing each angular momentum and composition and the resultant changes that occur in the stellar structure and nucleosynthesis. The distribution of angular momentum in the presupernova stage is of particular interest.

Two different one-dimensional hydrodynamic stellar evolution codes were modified to include angular momentum as a new local variable. The effects of centrifugal forces on the stellar structure were treated in latitudinally averaged way. Rotationally induced instabilities were included (Sect. 2.2): secular and dynamic shear instabilities, the Solberg-Høiland instability, the Eddington-Sweet circulation, and the Goldreich-Schubert-Fricke instability. The uncertain parameters of rotationally induced mixing were calibrated using observational constraints on the surface abundances (Sect. 3). Observed surface enrichments with CNO-processed matter were reproduced for stars in the mass range from $5\,\mathrm{M}_{\odot}$ to $60\,\mathrm{M}_{\odot}$, for typical initial stellar rotation rates. Stellar mass loss and its dependence on the surface rotation rate were also taken into account (Sect. 2.6).

The evolution of stars of approximately solar composition in the mass range from $10\,\mathrm{M}_{\odot}$ to $25\,\mathrm{M}_{\odot}$ was modeled up to iron core collapse, the immediate presupernova stage. Models that used different assumptions regarding the stabilizing effect of gradients in the mean molecular weight on rotationally induced instabilities were computed and compared. Observations indicate that gradients in the mean molecular weight inhibit rotationally induced mixing much less than in the pioneering models of Endal & Sofia (1978). This conclusion is also supported by recent investigations of the physics of meridional circulations, shear instabilities, and semiconvective mixing (Maeder & Zahn 1998).

12.1. Internal stellar structure

During central hydrogen burning, the products of the burning are mixed into the stellar envelope and new fuel is supplied to the convectively burning stellar core by rotationally induced mixing. Since this mixing proceeds on a time-scale comparable to the thermonuclear time-scale of hydrogen burning, a gradient of processed matter builds up inside the radiative envelope. The processed matter has a higher mean molecular weight, μ, than the pristine matter of the star, and therefore a gradient of the mean molecular weight results.

If rotationally induced mixing occurs by processes that depend sensitively upon these gradients, they act as a barrier (μ-barrier), and mixing between the core and the envelope is inhibited. Exactly when this inhibition becomes important depends on the initial angular momentum of the star. The amount of mixing that occurs between the core and the envelope is affected accordingly. Mixing inside the envelope also increases for larger initial angular momentum, since the dominant mixing process, Eddington-Sweet circulation, has an efficiency that increases as the square of the stellar rotation rate.

As the evolution of the star proceeds to later stages, the time-scale for rotationally induced mixing becomes too long in comparison to the evolutionary time-scales to constitute an important source of large-scale mixing. Also, the mixing is not able to dissolve the molecular weight barrier which forms in the core during central helium burning. In general, rotationally induced mixing does not strongly affect the stellar structure after central helium ignition. The evolution of the star from this point until core collapse is similar to that of a non-rotating star of same structure at this time, except for the differences in the nucleosynthesis discussed below.

For models where rotationally induced mixing is assumed to be insensitive to gradients in the mean molecular weight, no μ-barrier inhibits the mixing. This affects the mixing between the core and the envelope during central hydrogen burning. The μ-barrier in the superadiabatic part of the core during central helium burning is eroded by shear instabilities. Consequently, the convective core can grow unhindered. As a result, the helium cores are more massive, corresponding to non-rotating stars with about 25 % higher initial mass. Inside this helium core, the CO core is also larger than that of a non-rotating star with same helium core mass. Towards the end of central helium burning, fresh helium is mixed into the convective core both by the continuing growth of this core and by rotationally induced mixing. The fresh helium preferentially converts carbon into oxygen instead of producing new carbon by the triple-alpha process. This reduces the carbon abundance in the core. Except for this, the effect of rotationally induced mixing is small after helium ignition for the reason outlined above. In particular, also in this case, the hydrogen burning shell constitutes an efficient barrier for mixing processes — indeed even more efficient, because the core rotates slower as in the case where μ-gradients were considered (see below). A consequence of the enlarged cores is that the limit on the initial stellar mass for core collapse supernovae is somewhat smaller for higher initial rotation rates.

12.2. Angular momentum

At central hydrogen ignition, the stars establish almost uniform rotation. If a molecular weight barrier forms as hydrogen burning progresses, angular momentum is trapped inside the core and differential rotation results, with up to a factor of ~ 3 variation in the rotation rate between the core and the envelope. If μ-barriers are unimportant for the rotationally induced mixing, the stars stay close to rigid rotation until the end of central hydrogen burning. Since this barrier forms later in the faster rotators, stars having different initial rotation rates may end up with similar specific angular momenta in the core at the end of central hydrogen burning (Figs. 8D, 9C and D). Due to angular momentum transport during core helium burning, they may become even more similar in the pre-collapse stage (Fig. 12). Some angular momentum gets lost from the core during the restructuring that occurs after core hydrogen exhaustion, but during central helium burning the hydrogen-burning shell constitutes an efficient barrier that inhibits the transport of angular momentum out of the core. Even so, the average angular momentum of the core may decrease somewhat, since it grows into regions with lower specific angular momentum on top of it. The helium core itself stays close to uniform rotation (Figs. 8A and B). During central helium burning rotationally induced mixing processes already become slow compared to the evolution, and after core helium exhaustion they do not cause any relevant transport of angular momentum.

Only convective processes are rapid enough to notably redistribute angular momentum during the late stages of stellar evolution. Within the assumptions made, rigid rotation results in convective regions, transporting angular momentum from their bottom to their top. Subsequent phases of convective central and shell burning stages give some outward transport of angular momentum inside the carbon-oxygen core. Since none of the convective shells penetrates through the outer boundary of the CO core, the angular momentum remains trapped inside (Figs. 8F, 9E and F). The outer boundary of the helium core constitutes a similar barrier.

This has interesting consequence for the final angular momentum in the core. First, the different convective burning shells leave their fingerprint not only in the chemical composition, but also in the angular momentum distribution: a spiky profile results at the onset of core collapse (Fig. 12). The high peaks correspond to the upper edges of the most recently active convection zones and the deep valleys to their bottoms. Shells of similar composition tend to rotate almost rigidly. Second, even the slowest rotating core of the Type II supernova progenitor stars considered here would result in a neutron star rotating close to break-up if angular momentum were conserved during the collapse. This is not necessarily in contradiction with observations of young neutron stars in supernova remnants, even though the fastest of these rotates much slower. These pulsars are already hundreds of years old, and recent theoretical investigations of hot, newly born neutron stars indicate they may spin down to the observed rotation rates within about a year by emitting gravitational waves (Lindblom et al. 1998). The electro-magnetic radiation emanating from pulsars is trapped inside the supernova ejecta during that time, but the gravitational radiation of these very young neutron stars might become detectable in the future (Owen et al. 1998).

We are grateful to T.A. Weaver for helpful discussions and aid with KEPLER. This work was supported by the Deutsche Forschungsgemeinschaft through grants La 587/15 and La 587/16, by the the National Science Foundation (AST 97-31569), and by the Alexander von Humboldt Foundation. AH was, in part, supported by a “Doktorandenstipendium aus Mitteln des 2. Hochschulprogramms”.

References

Acheson, D.J. 1978, *Phil. Trans. Roy. Soc. London A*, **289**, 40.
Aksenov, A.G., Zabrodina, E.A., Imshennik, V.S., Nadezhin, D.K. 1997, *Astronomy letters*, **23**, 779.
Anders, E., Grevesse, N. 1989, *Geochim. Cosmochim. Acta*, **53**, 197.
Antia, H.M., Basu, S., Chitre, S.M. 1997, MNRAS, **298**, 543.
Baker, N., Kippenhahn, R. 1959, *ZfAp*, **48**, 140.
Beech, M., Mitalas, R. 1994, ApJS, **95**, 517.
Bernasconi, P.A., Maeder, A. 1996, A&A, **307**, 829.
Böhm-Vitense, E. 1958, *ZfAp*, **46**, 108.
Braun, H. 1997, PhD thesis, Ludwig-Maximilians-Universität München.
Chaboyer, B., Zahn, J.-P. 1992, A&A, **253**, 173.
Chin, C.-W., Stothers, R.B. 1991, ApJS, **77**, 299.
Chiosi, C., Maeder, A. 1986, *ARA&A*, submitted.
Clayton, D.D. 1968, *Principles of Stellar Evolution and Nucleosynthesis*, McGraw-Hill, New York.
Denissenkov, P.A. 1994, A&A, **287**, 113.
Eberl, T. 1997, private communication.
El Eid, M.F., Langer, N. 1986, A&A, **176**, 274.
Emden, R. 1907, *Gaskugeln: Anwendungen der mechanischen Wärmetheorie auf kosmologische und meteorologische Probleme*, Teubner, Leipzig.
Endal, A.S., Sofia, S. 1976, ApJ, **210**, 184.
Endal, A.S., Sofia, S. 1978, ApJ, **220**, 279.
Eryurt, D., Kırbıyık, H., Kızıloğlu, N., Civelek, R., Weiss, A. 1994, A&A, **282**, 485.
Fliegner, J. 1993, diploma thesis, Universitäts-Sternwarte Göttingen.
Fliegner, J., Langer, N., Venn, K. 1996, A&A, **308**, L13.
Fricke, K. 1968, *ZfAp*, **68**, 317.
Friend, D.B., Abbott, D.C. 1986, ApJ, **311**, 701.
Fukuda, I. 1982, PASP, **94**, 271.
Gies, D.R., Lambert, D.L. 1992, ApJ, **387**, 673.
Goldreich, P., Schubert, G. 1967, ApJ, **150**, 571.
Grevesse, N., Noels, A. 1993, in *Origin and Evolution of the Elements*, ed. N. Prantzo, E. Vangioni-Flam, M. Casse, Cambridge Univ. Press, Cambridge, p. 13.
Halbedel, E. 1996, PASP, **108**, 833.
Heger, A. 1998, PhD thesis, Technische Universität München.
Heger, A., Jeannin, L., Langer, N., Baraffe, I. 1997, A&A, **327**, 224.
Heger, A., Langer 1998, A&A, **334**, 210.
Herrero, A. 1994, *Space Sci. Rev.*, **66**, 137.

Herrero, A., Kudritzki, R.P., Vilchez, J.M., Kunze, D., Butler, K., Haser, S. 1992, A&A, **261**, 209.
Herrero, A., Villamariz, M.R., Martín, E.L. 1998, in *Proceedings of the 2nd Boulder-Munich Workshop on Hot Stars*, ed. I. Howarth et al., PASPC, **131**, p. 159.
Howarth, I.D., Siebert, K.W., Hussain, G.A.J., Prinja, R.K. 1997, MNRAS, **284**, 265.
Iglesias, C.A., Rogers, F.J. 1996, ApJ, **464**, 943.
Imshennik, V.S. 1995, *Space Sci. Rev.*, **74**, 325.
James, R.A., Kahn, F.D. 1970, A&A, **5**, 232.
James, R.A., Kahn, F.D. 1971, A&A, **12**, 332.
Kato, S. 1966, PASJ, **18**, 374.
Kippenhahn, R. 1969, A&A, **2**, 309.
Kippenhahn, R. 1974, in *Late Stages of Stellar Evolution*, ed. R.J. Taylor, J.E. Hesser, IAU Symp. 66, Reidel, Dortrecht, p. 20.
Kippenhahn, R., Meyer-Hofmeister, E., Thomas, H.C. 1970, ApJ, **5**, 155.
Kippenhahn, R., Thomas, H.-C. 1970, in *Stellar Rotation*, ed. A. Slettebak, IAU Coll. 4, Reidel, Dortrecht, p. 20.
Kippenhahn, R., Weigert, A. 1991, *Stellar Structure and Evolution*, Springer–Verlag, Berlin, 2nd edition.
Knobloch, E., Spruit, H.C. 1983, A&A, **125**, 59.
Kumar, P., Narayan, R., Loeb, A. 1995, ApJ, **453**, 480.
Lamers, H.J.G.M.L. 1993, in *Massive Stars: Their Lives in the Interstellar Medium*, ed. J.P. Cassinelli, E.B. Churchwell, ASPC, **35**, p. 517.
Lang, K.R. 1991, *Astrophysical Data*, Springer–Verlag, New York.
Langer, N. 1989, A&A, **220**, 135.
Langer, N. 1991, A&A, **252**, 669.
Langer, N. 1992, A&A, **265**, L17.
Langer, N. 1997, in *Luminous Blue Variables: Massive Stars in Transition*, ed. A. Nota, H.J.G.L.M. Lamers, ASPC, **120**, p. 83.
Langer, N. 1998, A&A, **329**, 551.
Langer, N., Heger, A., Woosley, S.E., Herwig, F. 1999, in *Nuclei in the Cosmos V*, ed. N. Prantzos, Édition Frontières, Paris, in press.
Langer, N., Kiriakidis, M., El Eid, M.F., Frick, K.J., Weiss, A. 1988, A&A, **192**, 177.
Langer, N., Sugimoto, D., Fricke, K.J. 1983, A&A, **126**, 207.
Lindblom, L., Owen, B.J., Morsink, S.M. 1998, Phys. Rev. Lett., **80**, 4843.
MacFadyen, A., Woosely, S.E. 1998, ApJ, in preparation.
Maeder, A. 1995, A&A, **299**, 84.
Maeder, A. 1997a, A&A, **321**, 134.
Maeder, A. 1997b, in *Proceedings of the 2nd Boulder-Munich Workshop on Hot Stars*, ed. I. Howarth et al., PASPC 131, p. 85.
Maeder, A., Meynet, G. 1996, A&A, **313**, 140.
Maeder, A., Zahn, J.-P. 1998, A&A, **334**, 1000.
Mashall, F.E., Gotthelf, E.V., Zhang, W., Middleditch, J., Wang, Q.D. 1998, astro-ph/9803214.
Mestel, L. 1952, MNRAS, **112**, 598.
Mestel, L. 1953, MNRAS, **113**, 716.
Meynet, G. 1997, in *Proceedings of the 2nd Boulder-Munich Workshop on Hot Stars*, ed. I. Howarth et al., PASPC 131, p. 96.
Meynet, G., Maeder, A. 1997, A&A, **321**, 465.
Munakata, H., Kohyama, Y., Itoh, N. 1985, ApJ, **296**, 197.
Nieuwenhuijzen, H., de Jager, C. 1990, A&A, **231**, 134.
Novikov, I. 1997, in *Stellar Remnants*, ed. G. Meynet, D. Schaerer, Saas Fee Advanced Course 25, Springer–Verlag, Berlin, p. 237.
Ostriker, J.P., Bodenheimer, P. 1973, ApJ, **180**, 171.
Ostriker, J.P., Tassuol, J.L. 1969, ApJ, **155**, 987.
Owen, B.J., Lindblom, L., Cutler, C., Schutz, B.F., Vecchio, A., Andersson, N. 1998, Phys. Rev. D, in press.
Owocki, S.P., Cranmer, S.R., Gayley, K.G. 1996, ApJ, **472**, L151.
Owocki, S.P., Gayley, K.G. 1997, in *Luminous Blue Variables: Massive Stars in Transition*, ed. A. Nota, H.J.G.L.M. Lamers, ASPC, **120**, p. 121.
Penny, L.R. 1996, ApJ, **463**, 737.
Pinsonneault, M.H., Kawaler, S.D., Sofia, S., Demarque, P. 1989, ApJ, **338**, 424.
Popham, R., Woosley, S.E., Fryer, C. 1998, ApJ, submitted.
Rampp, M., Müller, E., Ruffert, M. 1998, A&A, **332**, 969.
Richard, D., Zahn, J.-P. 1999, A&A, in press.
Schaller, G., Schaerer, D., Meynet, G., Maeder, A. 1992, *A&AS*, **96**, 269.
Shapiro, S.L., Teukolski, S.A. 1983, *Black Holes, White Dwarfs, and Neutron stars*, John Wiley, New York.
Slettebak, A. 1970, in *Stellar Rotation*, ed. A. Slettebak, Reidel, Dortrecht, p. 3.
Spitzer, L., J. 1962, *Physics of fully Ionized Gases*, Interscience Publ., New York.

Spruit, H.C. 1997, private communication.
Spruit, H.C., Knobloch, E., Roxburgh, I.W. 1984, Nature, **304**, 520.
Spruit, H.C., Phinney, E.S. 1998, Nature, **393**, 139.
Talon, S., Zahn, J.-P. 1997, A&A, **317**, 749.
Talon, S., Zahn, J.-P., Maeder, A., Meynet, G. 1997, A&A, **322**, 209.
Tassoul, J.-L. 1978, *Theory of Rotating Stars*, Princeton Univ. Press, Princeton.
Townsend, A.A. 1958, *J. Fluid Mech.*, **5**, 361.
Urpin, V.A., Shalybkov, D.A., Spruit, H.C. 1996, A&A, **306**, 455.
Venn, K.A., Lambert, D.L., Lemke, M. 1996, A&A, **307**, 894.
Vitense, E. 1953, *ZfAp*, **32**, 135.
von Zeipel, H. 1924a, MNRAS, **84**, 684.
von Zeipel, H. 1924b, MNRAS, **84**, 665.
Vrancken, M., Lennon, D.J., Dufton, P.L., Lambert, D.L. 1998, A&A, in preparation.
Wasiutyński, J. 1946, *Ap. Norveg.*, **4**, 1.
Weaver, T.A., Woosley, S.E. 1993, *Physics Reports*, **227**, 65.
Weaver, T.A., Woosley, S.E., Fuller, G.M. 1984, in *Numerical Astrophysics*, ed. J. Centrella, J. LeBlanc, R. Bowers, Jones and Bartlett, Boston, p. 374.
Weaver, T.A., Zimmerman, G.B., Woosley, S.E. 1978, ApJ, **225**, 1021.
Woosley, S.E. 1993, ApJ, **405**, 273.
Woosley, S.E. 1997, private communication.
Woosley, S.E., Weaver, T.A. 1988, *Physics Reports*, **163**, 79.
Zahn, J.-P. 1974, in *Stellar Instability and Evolution*, ed. P. Ledoux, A. Noels, A.W. Rogers, IAU Symp. 59, Reidel, Dortrecht, p. 185.
Zahn, J.-P. 1975, *Mem. Soc. Roy. Sci. Liège*, **8**, 31.
Zahn, J.-P. 1983, in *Processes in the Upper MS Stars*, ed. B. Hauck, A. Maeder, Saas-Fee Advanced Course 13, p. 253.
Zahn, J.-P. 1992, A&A, **265**, 115.
Zwerger, T., Müller, E. 1997, A&A, **320**, 209.

A. Improvement of hydrogen burning in the KEPLER code

The treatment of nuclear burning in KEPLER was improved by taking into account neutrino losses and corrections to the energy released during hydrogen burning.

In general, until oxygen burning, KEPLER calculates the nuclear energy generation rate by simple subtraction of the total nuclear binding energy of the composition before and after a time-step. However, during hydrogen burning weak interactions are present, with implications for the energy generation which do not occur in other pre-oxygen burning stages. In particular, the mass difference of n and $\mathsf{p}+\mathsf{e}^-$ of $782.3\,\mathrm{MeV\,c^{-2}}$ has to be taken into account. This reduces the energy release per $^4\mathsf{He}$ formed by twice that value, i.e., from 28.296 MeV for the binding energy of two protons and two neutrons, to 26.731 MeV for the total difference in rest mass. That is a relative reduction of the energy generation rate of hydrogen burning by 5.85 %.

Additionally, within the CNO main cycle the weak reaction $^{13}\mathsf{N}(\beta^+\nu_\mathrm{e})^{13}\mathsf{C}$ releases in average 0.71 MeV in the form of neutrinos, $^{15}\mathsf{O}(\beta^+\nu_\mathrm{e})^{15}\mathsf{N}$ releases 1.0 MeV, and the reaction $^{17}\mathsf{F}(\beta^+\nu_\mathrm{e})^{17}\mathsf{O}$ of the secondary CNO cycle, which has a probability of only $\sim 10^{-4}$ relative to the main cycle, 0.94 MeV (Clayton 1968). On average, 1.71 MeV are lost due to neutrinos for each four $^1\mathsf{H}$ burned, reducing the effective energy release by another 6.4 % from 26.731 MeV to about 24.97 MeV per $^4\mathsf{He}$ formed. KEPLER was also corrected for the appropriate neutrino losses of the three pp chains, but they do not contribute in the high-mass stars of the present work.

These two effects sum up to a total reduction of the energy release of hydrogen burning by 13.32 %. However, this alters the structure of zero-age main sequence stars only slightly, since the energy generation rate for CNO hydrogen burning depends on a high power of the temperature (16 to 18) and thus a slight increase of the central temperature compensates the lower energy generation rate. The nucleosynthesis, as far as the ratios of the CNO isotopes are concerned, are not altered notably by the higher temperature.

The lower total energy release of hydrogen burning reduces the lifetime of the star during central hydrogen burning by about the same factor. The convective mixing in the core is not affected by the smaller duration of central hydrogen burning, since the convective mixing time-scale is still much shorter. For mixing processes which act on a time-scale comparable to that of central hydrogen burning, e.g., semiconvection, the reduction of the main sequence lifetime can become noticeable. It is particularly important for rotationally induced mixing and mass loss from the stellar surface. Mass loss rates mostly depend only on stellar surface properties (Sect. 2.6) and thus, to first approximation, the total mass loss scales with the evolutionary time-scale. The stellar angular momentum loss from the surface is also altered by this and the amount of products of hydrogen burning exposed to the surface of the star depends on both the time available for the rotationally induced mixing processes to transport them to the surface and the amount of matter removed from the surface. Furthermore, a higher angular momentum loss from the surface can introduce more shear and correspondingly more mixing.

After termination of core hydrogen burning, hydrogen continues burning in a shell above the helium core. Since the stellar structure determines the rate at which energy has to be released by hydrogen burning, more hydrogen is burned in order to release the same amount of energy using the corrected energy generation rate. This increases the rate at which the helium core grows and thus its final size.

In all models computed with KEPLER in the present work, the corrected treatment of hydrogen burning was employed.

B. Diagrams for the evolution of the internal stellar structure

The "Kippenhahn diagrams" of this Appendix show the convective structure and the nuclear energy generation rate as a function of time for selected model sequences. In these plots the time-axis gives the logarithm of the time left until core collapse (in yr). From the infall velocities occurring in the last computed models and from the radius at which the maximum infall velocity occurs ($\sim 10^3\,\mathrm{km\,s^{-1}}$ and $10^3\,\mathrm{km}$, respectively) we estimated $10^{-7.5}\,\mathrm{yr}$ ($\sim 1\,\mathrm{s}$) for the time until "core bounce".

The y-axis gives the (interior) mass coordinate, m, in units of the solar mass. The total mass of the star is indicated by a thick solid line and shows the mass loss from the stellar surface. Note that because of the way the time-axis is chosen, the slope of this curve does not directly correspond to the mass loss rate.

Diagonal hatching indicates convective regions. In order to better visualize the boundaries of convection zones they are framed by thin lines. Semiconvection is indicated by narrow cross-hatching.

The net nuclear contribution to the energy generation rate including neutrino losses are shown as grey shading. Increasingly darker grey scale levels correspond to increasing orders of magnitude of the energy generation rate. The lightest grey shows regions with an energy generation rate of $10^{-1}\,\mathrm{erg\,g^{-1}\,s^{-1}}$ or more, the next darker shade of grey underlies regions with an energy generation rate of $10^{0}\,\mathrm{erg\,g^{-1}\,s^{-1}}$ or above, and so forth.

The sequence of central convective burning phases is (from left to right) hydrogen, helium, carbon, neon, oxygen, and silicon burning.

isotope	mass fraction	isotope	mass fraction	isotope	mass fraction
^{1}H	$7.00\cdot10^{-1}$	^{14}N	$1.07\cdot10^{-3}$	^{24}Mg	$5.60\cdot10^{-4}$
^{3}He	$3.78\cdot10^{-5}$	^{15}N	$3.92\cdot10^{-6}$	^{25}Mg	$7.09\cdot10^{-5}$
^{4}He	$2.80\cdot10^{-1}$	^{16}O	$1.04\cdot10^{-3}$	^{26}Mg	$7.81\cdot10^{-5}$
^{6}Li	$6.69\cdot10^{-10}$	^{17}O	$3.95\cdot10^{-6}$	^{27}Al	$6.24\cdot10^{-5}$
^{7}Li	$9.63\cdot10^{-9}$	^{18}O	$2.08\cdot10^{-5}$	^{28}Si	$7.08\cdot10^{-4}$
^{9}Be	$1.72\cdot10^{-10}$	^{19}F	$3.89\cdot10^{-7}$	^{29}Si	$3.58\cdot10^{-5}$
^{10}B	$1.04\cdot10^{-9}$	^{20}Ne	$1.77\cdot10^{-3}$	^{30}Si	$2.37\cdot10^{-5}$
^{11}B	$4.92\cdot10^{-9}$	^{21}Ne	$4.31\cdot10^{-6}$	^{56}Fe	$1.37\cdot10^{-3}$
^{12}C	$3.62\cdot10^{-3}$	^{22}Ne	$1.29\cdot10^{-4}$		
^{13}C	$4.03\cdot10^{-5}$	^{23}Na	$3.60\cdot10^{-5}$		

Table 1: Initial isotopic mass fractions for the models computed with the STERN code (Sect. 4.1). They are taken from Grevesse & Noels (1993). The initial abundances of the radioactive isotopes ^{7}Be, ^{8}B, ^{11}C, ^{12}N, and ^{26}Al, and that of ^{2}H are set to zero.

isotope	mass fraction	isotope	mass fraction	isotope	mass fraction
^{1}H	$7.0000 \cdot 10^{-1}$	^{16}O	$1.0175 \cdot 10^{-2}$	^{36}Ar	$1.0176 \cdot 10^{-4}$
^{3}He	$2.9798 \cdot 10^{-5}$	^{20}Ne	$1.8545 \cdot 10^{-3}$	^{40}Ca	$6.9515 \cdot 10^{-5}$
^{4}He	$2.7997 \cdot 10^{-1}$	^{24}Mg	$7.3366 \cdot 10^{-4}$	^{48}Cr	$3.1177 \cdot 10^{-6}$
^{12}C	$3.2467 \cdot 10^{-3}$	^{28}Si	$8.1332 \cdot 10^{-4}$	^{52}Fe	$1.9180 \cdot 10^{-5}$
^{14}N	$1.1732 \cdot 10^{-3}$	^{32}S	$4.5056 \cdot 10^{-4}$	^{54}Fe	$1.3594 \cdot 10^{-3}$

Table 2: Initial isotopic mass fractions for the models computed with the KEPLER code (Sect. 4.2). The initial abundances of the radioactive isotopes ^{44}Ti and ^{56}Ni, which are also in the network, are set to zero.

model	$M_{\rm initial}$ $\mathrm{M}_\odot$	$J_{\rm initial}$ $10^{52}\,\mathrm{erg\,s}$	$v_{\rm ZAMS}$ $\mathrm{km\,s^{-1}}$	$f_{\rm c}$	f_μ	evolution followed until
D10	10	0	0	–	–	carbon shell burning
D12	12	0	0	–	–	off-center neon burning
D15	15	0	0	–	–	core collapse
D20	20	0	0	–	–	core collapse
D25	25	0	0	–	–	core collapse
E08	8	0.53	205	0.01	0	carbon shell burning
E10	10	0.80	207	0.01	0	core collapse
E12	12	1.10	206	0.01	0	core collapse
E15	15	1.60	206	0.01	0	core collapse
E20	20	2.50	201	0.01	0	core collapse
E25	25	3.50	205	0.01	0	core collapse
G12	12	0.55	100	0.01	0	core hydrogen exhaustion
F12	12	1.65	327	0.01	0	core hydrogen exhaustion
E12B	12	1.10	206	1/30	0.05	off-center neon burning
E15B	15	1.60	206	1/30	0.05	core collapse
E20B	20	2.50	201	1/30	0.05	core collapse
F12B	12	1.65	328	1/30	0.05	carbon shell burning
F15B	15	2.40	323	1/30	0.05	core collapse
F20B	20	3.75	307	1/30	0.05	core collapse
G12B	12	0.55	99	1/30	0.05	carbon shell burning
G15B	15	0.80	102	1/30	0.05	core collapse
G20B	20	1.25	103	1/30	0.05	core collapse
H12B	12	2.20	474	1/30	0.05	carbon shell burning
H15B	15	3.20	457	1/30	0.05	core hydrogen exhaustion
H20B	20	5.00	425	1/30	0.05	core helium burning

Table 3: Parameters of the model sequences. Shown are the model name (left column), the initial mass $M_{\rm initial}$, the initial angular momentum $J_{\rm initial}$, the equatorial rotational velocity at the surface at central hydrogen ignition $v_{\rm ZAMS}$, and two parameters of rotationally induced mixing, $f_{\rm c}$ and f_μ. The last column gives the final evolutionary stage to which the models are evolved.

central burning phase	E15				E15B			
	τ^*_{KH} yr	$\omega/\omega_{\mathrm{Kep}}$	τ_{ES} yr	τ_{burn} yr	τ^*_{KH} yr	$\omega/\omega_{\mathrm{Kep}}$	τ_{ES} yr	τ_{burn} yr
hydrogen	$5{\cdot}10^4$	$5{\cdot}10^{-2}$	$2{\cdot}10^7$	$1{\cdot}10^7$	$5{\cdot}10^4$	$5{\cdot}10^{-2}$	$2{\cdot}10^7$	$1{\cdot}10^7$
helium	$5{\cdot}10^4$	$2{\cdot}10^{-2}$	$1{\cdot}10^8$	$1{\cdot}10^6$	$7{\cdot}10^4$	$6{\cdot}10^{-2}$	$2{\cdot}10^7$	$1{\cdot}10^6$
carbon	$4{\cdot}10^4$	$3{\cdot}10^{-2}$	$4{\cdot}10^7$	$4{\cdot}10^2$	$6{\cdot}10^4$	$8{\cdot}10^{-2}$	$9{\cdot}10^6$	$4{\cdot}10^3$
oxygen	10	$5{\cdot}10^{-2}$	$3{\cdot}10^3$	1	30	0.1	$3{\cdot}10^3$	5
silicon	0.3	$8{\cdot}10^{-2}$	50	$1{\cdot}10^{-2}$	0.3	0.2	$1{\cdot}10^1$	$3{\cdot}10^{-2}$

Table 4: Values of the Kelvin-Helmholtz time-scale τ^*_{KH} (Eq. 37), the ratio of angular velocity to the Keplerian angular velocity $\omega/\omega_{\mathrm{Kep}}$, the Eddington-Sweet circulation time-scale τ_{ES} (Zahn 1992), and the burning time-scale τ_{burn} for the core region during the major nuclear burning phases, for models `E15` (left) and `E15B` (right).

model	$M_{\rm initial}$ $\mathrm{M}_\odot$	$M_{\rm final}$ $\mathrm{M}_\odot$	$M_{\sf He}$ $\mathrm{M}_\odot$	$M_{\sf C/O}$ $\mathrm{M}_\odot$	$M_{\sf Fe}$ $\mathrm{M}_\odot$	$v_{\rm ZAMS}$ $\mathrm{km\,s^{-1}}$	$J_{\rm initial}$ erg s	$J_{\rm final}$ erg s	$J_{\sf He}$ erg s	$J_{\sf C/O}$ erg s	$J_{\sf Fe}$ erg s	$j_{\sf Fe}$ $\mathrm{cm^2\,s^{-1}}$
`D10`	10	9.61	1.24^a	1.22	$-^b$	0	0	0	0	0	0	0
`D12`	12	11.42	2.85	1.42	$-^b$	0	0	0	0	0	0	0
`D15`	15	13.55	3.82	1.77	1.33	0	0	0	0	0	0	0
`D20`	20	16.31	5.68	2.31	1.64	0	0	0	0	0	0	0
`D25`	25	18.72	7.86	3.11	1.36	0	0	0	0	0	0	0
`E08`	8	7.65	1.38^a	1.35	$-^b$	205	$5.30{\cdot}10^{51}$	$2.49{\cdot}10^{51}$	$2.40{\cdot}10^{49}$	$2.36{\cdot}10^{49}$	$-^b$	$-^b$
`E10`	10	9.23	2.84	1.78	1.36	207	$8.00{\cdot}10^{51}$	$2.09{\cdot}10^{51}$	$8.04{\cdot}10^{49}$	$3.89{\cdot}10^{49}$	$2.13{\cdot}10^{49}$	$7.87{\cdot}10^{15}$
`E12`	12	10.35	3.63	2.37	1.34	206	$1.10{\cdot}10^{52}$	$1.29{\cdot}10^{51}$	$1.20{\cdot}10^{50}$	$5.32{\cdot}10^{49}$	$1.50{\cdot}10^{49}$	$5.63{\cdot}10^{15}$
`E15`	15	10.86	5.10	3.40	1.46	206	$1.60{\cdot}10^{52}$	$1.38{\cdot}10^{51}$	$2.30{\cdot}10^{50}$	$1.15{\cdot}10^{50}$	$1.86{\cdot}10^{49}$	$6.40{\cdot}10^{15}$
`E20`	20	11.00	7.71	5.01	1.73	201	$2.50{\cdot}10^{52}$	$7.15{\cdot}10^{50}$	$3.95{\cdot}10^{50}$	$1.82{\cdot}10^{50}$	$1.92{\cdot}10^{49}$	$5.58{\cdot}10^{15}$
`E25` ^{c}	25	5.45	5.45	4.07	1.69	205	$3.50{\cdot}10^{52}$	$1.40{\cdot}10^{50}$	$1.40{\cdot}10^{50}$	$7.52{\cdot}10^{49}$	$1.05{\cdot}10^{49}$	$3.12{\cdot}10^{15}$
`G12B`	12	11.32	2.68	1.41	$-^b$	99	$5.50{\cdot}10^{51}$	$3.07{\cdot}10^{51}$	$1.15{\cdot}10^{50}$	$4.18{\cdot}10^{49}$	$-^b$	$-^b$
`G15B`	15	13.46	3.63	1.79	1.34	102	$8.00{\cdot}10^{51}$	$3.99{\cdot}10^{51}$	$2.36{\cdot}10^{50}$	$6.80{\cdot}10^{49}$	$3.28{\cdot}10^{49}$	$1.23{\cdot}10^{16}$
`G20B`	20	16.03	5.55	2.61	1.38	103	$1.25{\cdot}10^{52}$	$3.49{\cdot}10^{51}$	$5.33{\cdot}10^{50}$	$1.24{\cdot}10^{50}$	$3.13{\cdot}10^{49}$	$1.14{\cdot}10^{16}$
`E12B`	12	11.25	2.72	1.46	$-^b$	206	$1.10{\cdot}10^{52}$	$4.92{\cdot}10^{51}$	$1.29{\cdot}10^{50}$	$4.94{\cdot}10^{49}$	$-^b$	$-^b$
`E15B`	15	13.26	3.69	1.89	1.40	206	$1.60{\cdot}10^{52}$	$6.96{\cdot}10^{51}$	$2.73{\cdot}10^{50}$	$8.77{\cdot}10^{49}$	$4.07{\cdot}10^{49}$	$1.46{\cdot}10^{16}$
`E20B`	20	15.19	5.71	2.69	1.38	201	$2.50{\cdot}10^{52}$	$5.10{\cdot}10^{51}$	$6.36{\cdot}10^{50}$	$1.55{\cdot}10^{50}$	$3.47{\cdot}10^{49}$	$1.26{\cdot}10^{16}$
`F12B`	12	10.93	3.04	1.61	$-^b$	328	$1.65{\cdot}10^{52}$	$3.43{\cdot}10^{51}$	$1.72{\cdot}10^{50}$	$5.98{\cdot}10^{49}$	$-^b$	$-^b$
`F15B`	15	12.89	3.88	2.01	1.38	323	$2.40{\cdot}10^{52}$	$7.90{\cdot}10^{51}$	$3.01{\cdot}10^{50}$	$9.69{\cdot}10^{49}$	$3.66{\cdot}10^{49}$	$1.33{\cdot}10^{16}$
`F20B`	20	14.76	5.99	2.75	1.36	307	$3.75{\cdot}10^{52}$	$5.45{\cdot}10^{51}$	$7.42{\cdot}10^{50}$	$1.71{\cdot}10^{50}$	$3.71{\cdot}10^{49}$	$1.37{\cdot}10^{16}$
`H12B`	12	9.77	3.81	1.78	$-^b$	474	$2.20{\cdot}10^{52}$	$1.41{\cdot}10^{51}$	$2.59{\cdot}10^{50}$	$6.93{\cdot}10^{49}$	$-^b$	$-^b$

Table 5: Properties of the final models of various sequences. Listed are the initial and final stellar mass, $M_{\rm initial}$ and $M_{\rm final}$, the final masses of the helium core $M_{\sf He}$, of the carbon/oxygen core $M_{\sf C/O}$ and of the iron core $M_{\sf Fe}$. Then, the equatorial surface rotation velocity at core hydrogen ignition, $v_{\rm ZAMS}$, is given. Furthermore, the initial stellar angular momentum is given, and the final angular momentum of the star and the helium, CO and iron cores. In the last column the average specific angular momentum in the iron core is shown.

[a] dredge-up of helium core [b] not evolved to pre-collapse stage [c] star becomes a Wolf-Rayet star during central helium burning

evolutionary state	$J(m)/m$ $\mathrm{cm^2\,s^{-1}}$	r cm	ρ_c $\mathrm{g\,cm^{-3}}$	ω $\mathrm{rad\,s^{-1}}$	$\omega/\omega_\mathrm{Kep}$
H ignition	$5.5{\cdot}10^{16}$	$5.8{\cdot}10^{10}$	4.8	$5.0{\cdot}10^{-5}$	$4.6{\cdot}10^{-2}$
H exhaustion	$1.0{\cdot}10^{16}$	$4.3{\cdot}10^{10}$	12.5	$1.6{\cdot}10^{-5}$	$1{\cdot}10^{-2}$
He exhaustion	$6.5{\cdot}10^{15}$	$7.2{\cdot}10^{9}$	$3{\cdot}10^{3}$	$3.8{\cdot}10^{-4}$	$1.5{\cdot}10^{-2}$
pre-collapse	$5.6{\cdot}10^{15}$	$2.2{\cdot}10^{8}$	$3.9{\cdot}10^{9}$	$3.7{\cdot}10^{-1}$	0.08
neutron star	$(5{\cdot}10^{15})$	$(1.2{\cdot}10^{6})$	$\sim 4{\cdot}10^{14}$	$1{\cdot}10^{4}$	0.9

Table 6: Evolution of the radius, r, the angular velocity, ω, and its ratio to the Keplerian rotational velocity, $\omega_\mathrm{Kep} = \sqrt{Gm/r^3}$, all at a mass coordinate of $m = 1.7\,\mathrm{M_\odot}$, and the mass of the iron core at core collapse of Model E20. The second column gives the specific angular momentum $J(m)/m$ of the inner $1.7\,\mathrm{M_\odot}$. The central density ρ_c is given for comparison. The initial model has a mass of $20\,\mathrm{M_\odot}$ and a ZAMS rotational velocity of $\sim 200\,\mathrm{km\,s^{-1}}$. Assuming that the neutron star gets a radius of about 12 km and retains about the angular momentum of the iron core at core collapse, it evolves close to critical rotation. It is assumed that the moment of inertia of the rigidly rotating neutron star of radius R and mass M is given by $0.8\frac{2}{5}MR^2$. The geometrical factor $\frac{2}{5}$ corresponds to a solid sphere of constant density, and the numerical factor 0.8 is found from a neutron star model provided by Eberl (1997).

pulsar	period ms	j ($R = 12\,\mathrm{km}$) $\mathrm{cm^2\,s^{-1}}$
PSR B0531+21 (Crab)	33	$8.8{\cdot}10^{13}$
PSR B0540-69 (LMC)	50	$5.8{\cdot}10^{13}$
PSR B1509-58	150	$1.9{\cdot}10^{13}$
PSR J0537-6910 (N157B; LMC)	16	$1.8{\cdot}10^{14}$

Table 7: Rotational periods of known young pulsars associated with supernova remnants (Mashall et al. 1998) and their specific angular momentum $j = J/M$ for an assumed radius of $R = 12\,\mathrm{km}$, if rigid rotation and a moment of inertia of $I = 0.32MR^2$ is assumed (see Table 6).

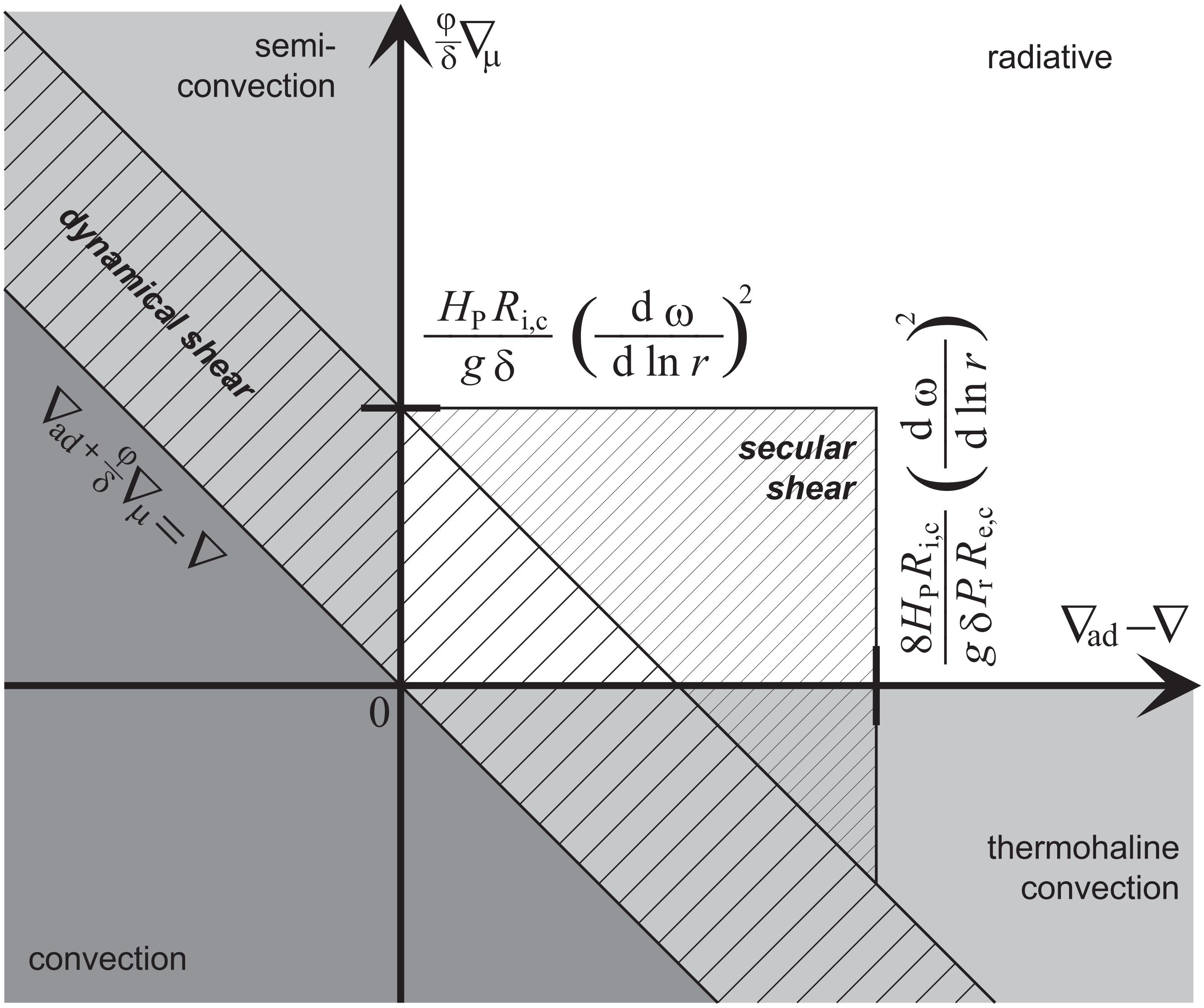

Fig. 1.— Schematic representation of the regions of different instabilities in a plane spanned by the stabilizing sub-adiabatic temperature gradient (horizontal axis), and the stabilizing mean molecular weight gradient ∇_μ (vertical axis). Both axes have identical units. Convection is indicated by dark grey shading, semiconvection (at positive mean molecular weight gradients) and thermohaline convection (at negative μ-gradients) are displayed by light grey shading. The radiatively stable regime is shown in white. Rotationally induced instabilities are indicated by hatched areas. The dynamical shear instability (wide thick hatching) acts only up to a certain distance to the Ledoux-unstable region, which is determined by the amount of shear (Fig. 2). The secular shear instability (narrow fine hatching) can penetrate in regions further away from the convective instability since it allows for thermal adjustment of displaced mass elements. It can also penetrate into the region of stabilizing μ-gradients, but to a much smaller extent since usually in stars it is $8/(\mathrm{Pr}\,R_{\mathrm{e,c}}) \gg 1$ ($R_{\mathrm{e,c}}$ is the critical Reynolds number and Pr the Prandtl-number; cf. Sections 2.3.1 and 2.3.3).

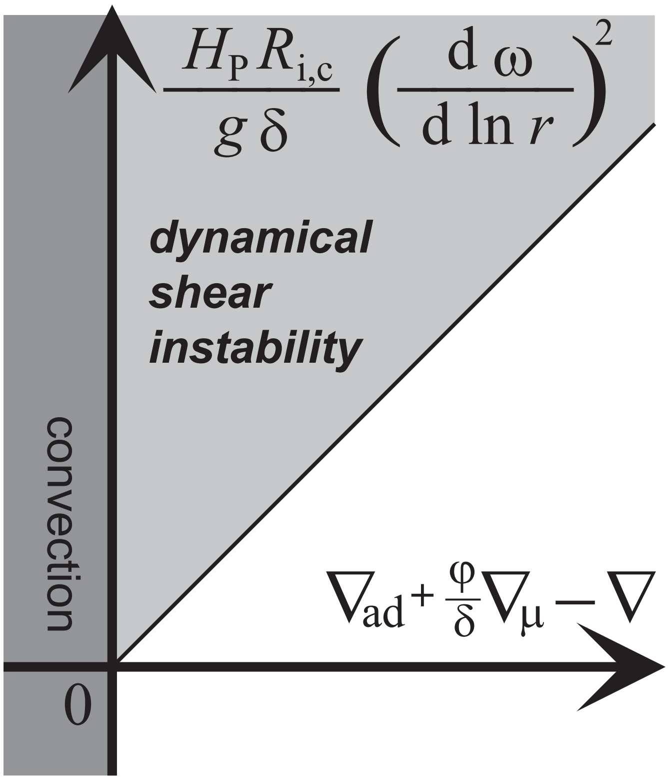

Fig. 2.— Region of instability due to dynamical shear (light grey) in the plane of stabilizing temperature and composition stratification (horizontal axis) and destabilizing shear (vertical axis). Both axes have the same units. Instability due to convection is indicated by dark grey shading. See also Fig. 1.

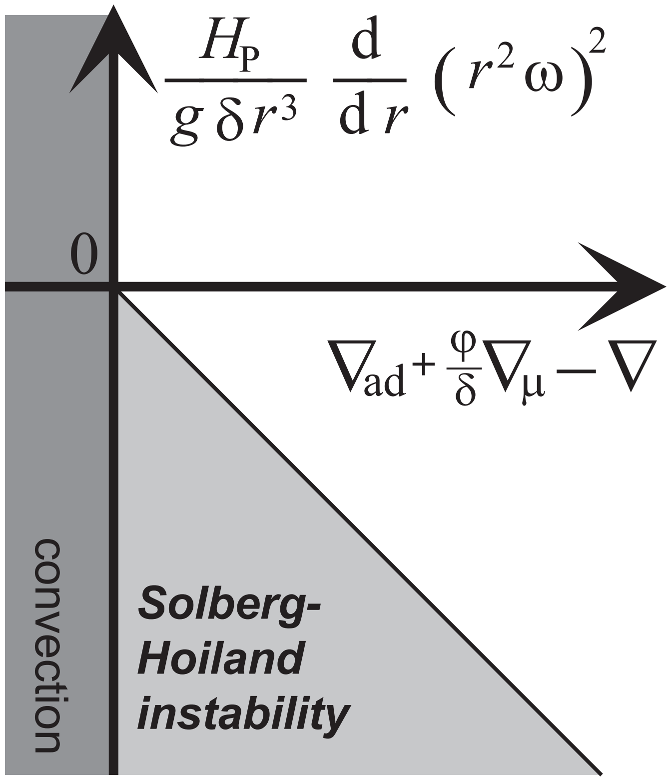

Fig. 3.— Region of instability according to the Solberg-Høiland criterion (light grey) in the plane of stabilizing temperature and composition stratification (horizontal axis) and stabilizing increasing specific angular momentum ($j \sim r^2\omega$) (vertical axis). Both axes have identical units. Instability due to convection is indicated by dark grey shading. The Solberg-Høiland instability can occur in regions where the specific angular momentum decreases outwards.

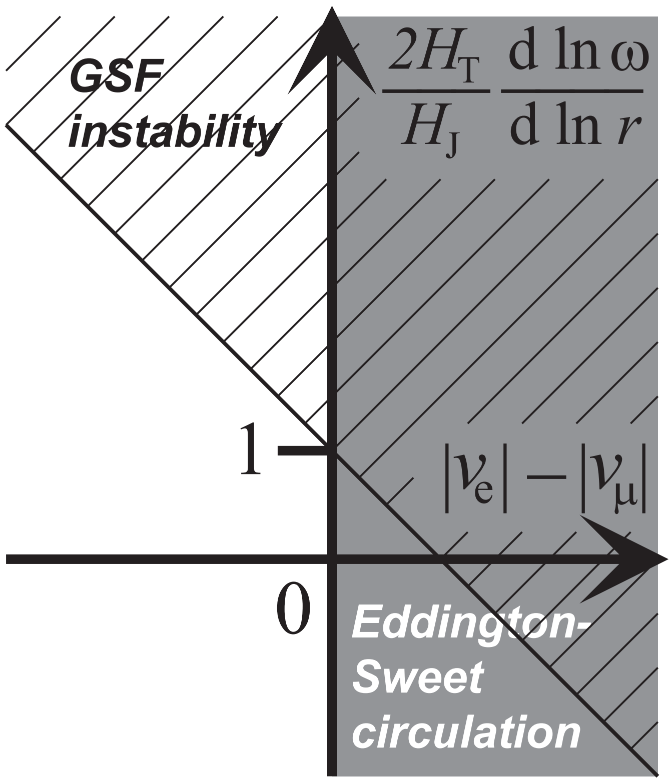

Fig. 4.— Region of instability due to Eddington-Sweet circulation (dark grey) and the Goldreich-Schubert-Fricke instability (hatching) in the plane of residual Eddington-Sweet circulation velocity (horizontal axis) and the factor v_g/v_e (vertical axis) of Goldreich-Schubert-Fricke velocity relative to Eddington-Sweet circulation velocity in the absence of μ-gradients. The boundary of the GSF-unstable region intersects the x-axis at $|v_e| - |v_\mu| = |v_e|$, i.e., where $|v_\mu| = 0$.

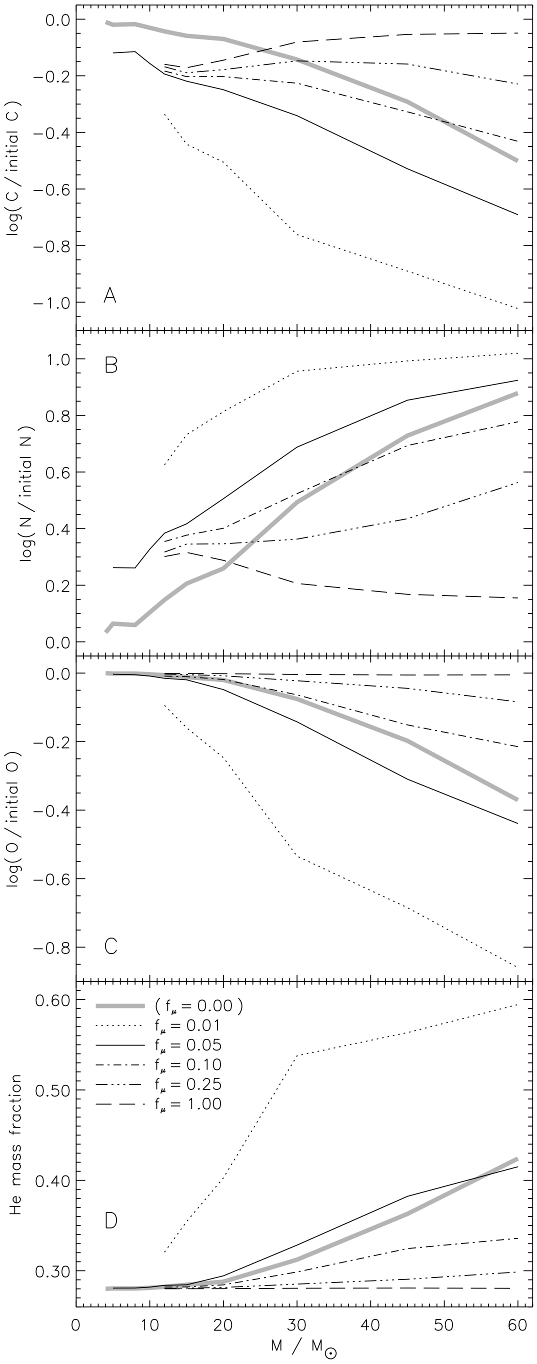

Fig. 5.— Surface abundances at core hydrogen exhaustion as function of the initial stellar mass for models with an equatorial surface rotation rate of $\sim 200\,\mathrm{km\,s^{-1}}$ at hydrogen ignition. Thin lines correspond to different values of f_μ (Sect. 3) for fixed $f_\mathrm{c} = 1/30$. The thick grey line corresponds to $f_\mathrm{c} = 1/100$ and $f_\mu = 0$. In Panels **A**–**C**, the change of the mass fractions of carbon, nitrogen, and oxygen, respectively, relative to the initial values are shown; Panel **D** shows the surface helium mass fractions. Models with initial masses of $12\,\mathrm{M}_\odot$, $15\,\mathrm{M}_\odot$, $20\,\mathrm{M}_\odot$, $30\,\mathrm{M}_\odot$, $45\,\mathrm{M}_\odot$, and $60\,\mathrm{M}_\odot$ have been calculated with the KEPLER code. For $f_\mu = 0.05$ (solid thin line) and $f_\mu = 0$ (grey thick line), additionally $5\,\mathrm{M}_\odot$, $8\,\mathrm{M}_\odot$, and $10\,\mathrm{M}_\odot$ stars are computed, and for the case $f_\mu = 0$ also a $4\,\mathrm{M}_\odot$ model is calculated.

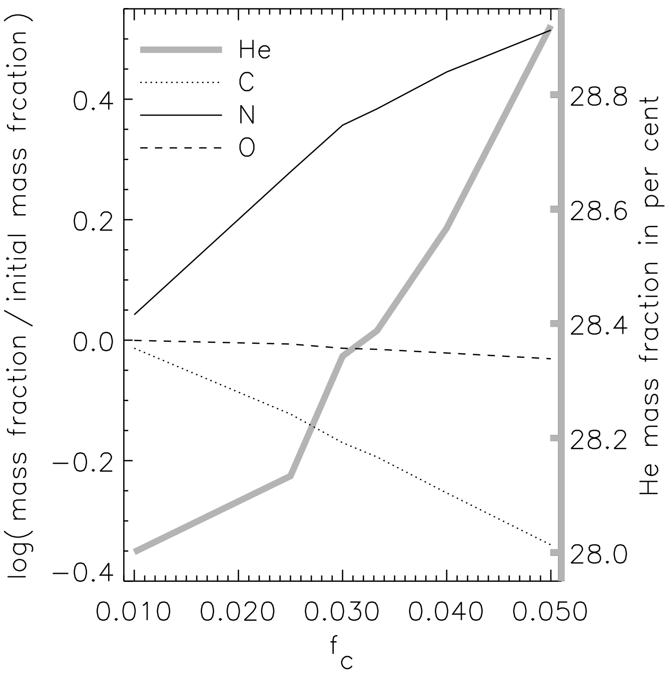

Fig. 6.— Surface abundances at core hydrogen exhaustion as a function of f_c, for $12\,M_\odot$ stars with an equatorial rotational velocity at the surface of $\sim\,200\,\mathrm{km\,s^{-1}}$ at hydrogen ignition. The thin dotted, solid, and dashed lines give the logarithm of the surface abundance of carbon, nitrogen, and oxygen, respectively, relative to their initial values (left scale). The thick grey line shows the surface mass fraction of helium (right scale). Model sequences have been computed for $f_c = 0.01$, 0.025, 0.03, 1/30, 0.04 and 0.05 with the KEPLER code.

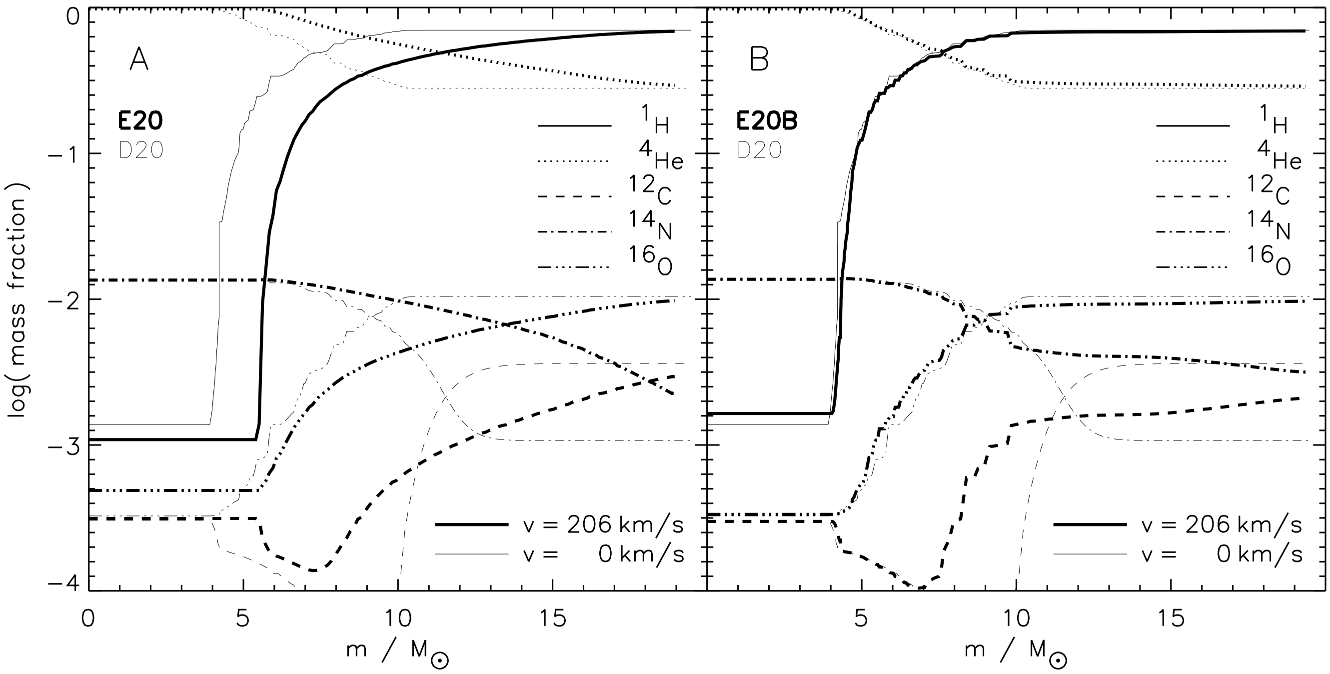

Fig. 7.— Mass fractions of different isotopes as a function of the mass coordinate m at core hydrogen exhaustion. Compared are the chemical structures of rotating (thick lines) and a non-rotating (thin lines; same in both Panels; Model `D20`) $20\,\mathrm{M}_\odot$ models. The rotating models have a ZAMS equatorial rotational velocity of $\sim\ 200\,\mathrm{km\,s^{-1}}$. Panel **A**: Model `E20`, where rotationally induced mixing is *not* inhibited by μ-gradients. Panel **B**: Model `E20B`, where rotationally induced mixing is inhibited by μ-gradients ($f_\mu = 0.05$).

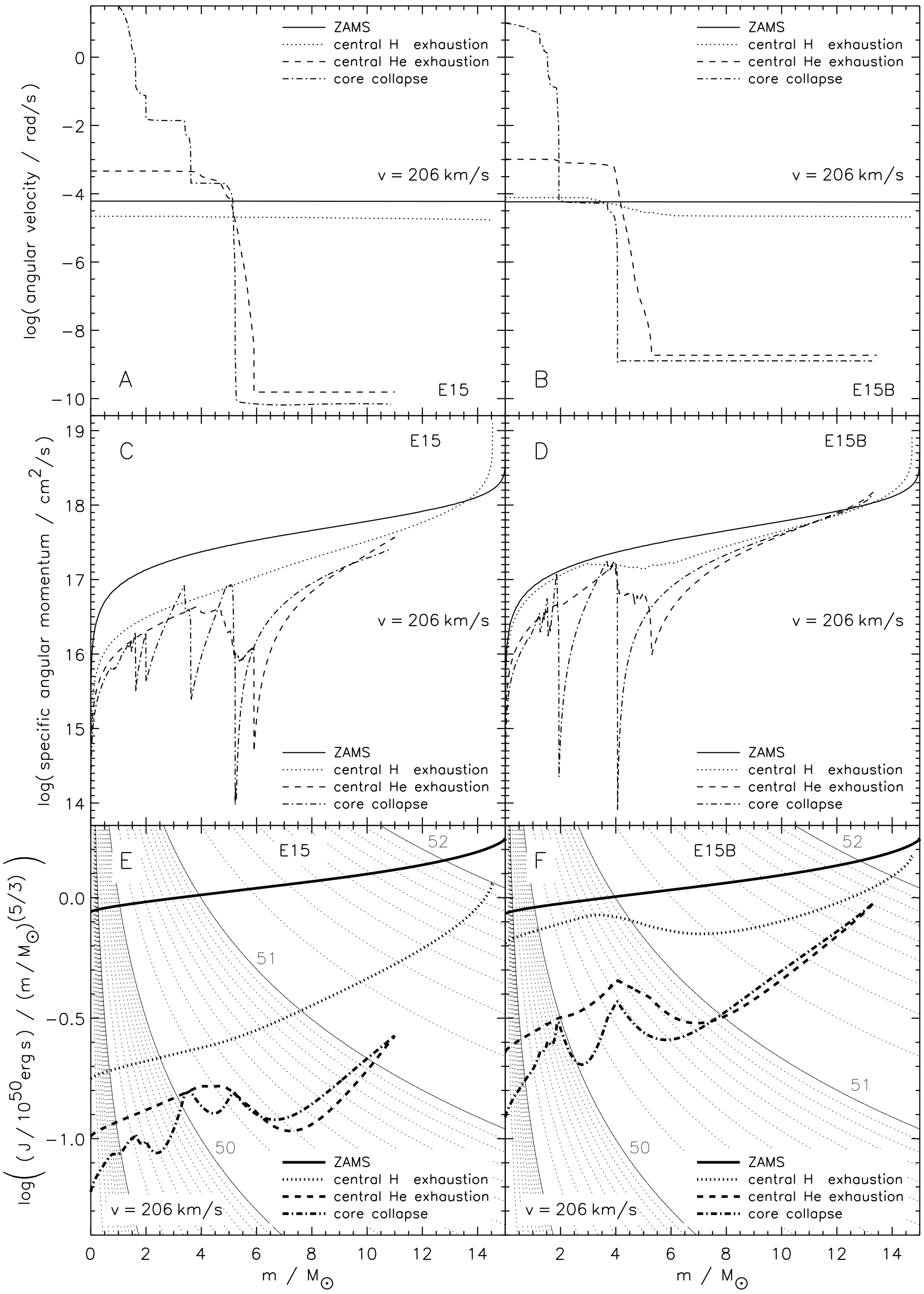

Fig. 8.— Angular velocity (Panels **A** and **B**), specific angular momentum (Panels **C** and **D**), and integrated angular momentum, $J(m) = \int_0^m j(m')\,\mathrm{d}m'$, divided by $m^{5/3}$ (thick lines; Panels **E** and **F**) as a function of the mass coordinate m at different evolutionary stages for two $15\,\mathrm{M}_\odot$ stars with a ZAMS equatorial rotational velocity of $\sim 200\,\mathrm{km\,s^{-1}}$. Panels **A**, **C**, and **E** show Model `E15` (inefficient μ-barrier), and Panels **B**, **D**, and **F** Model `E15B` (efficient μ-barrier). The thin lines in Panels **E** and **F** give a logarithmic scale of levels of constant J, labeled with $\log\,(J/\mathrm{erg\,s})$.

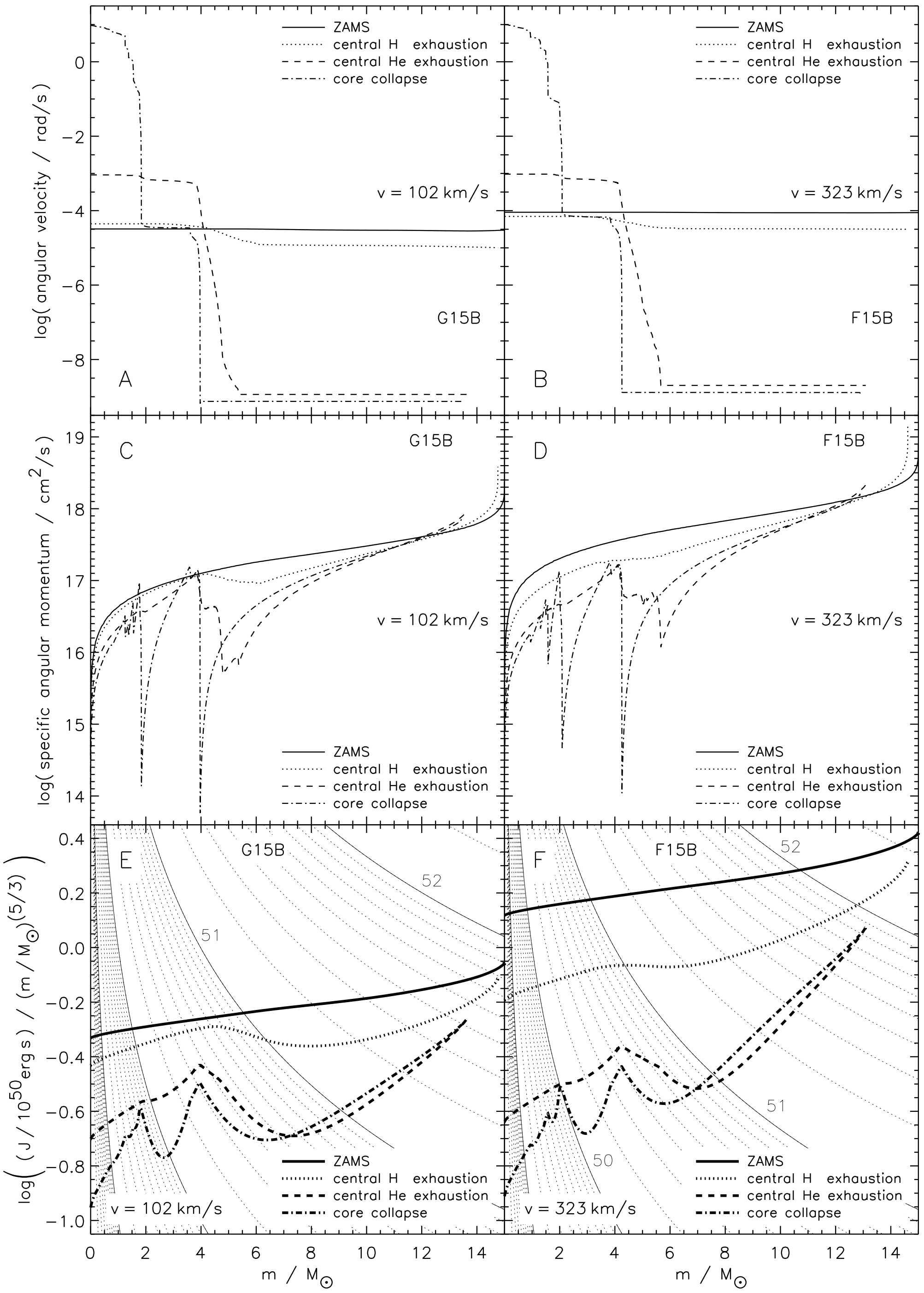

Fig. 9.— Angular velocity (Panels **A** and **B**), specific angular momentum (Panels **C** and **D**), and integrated angular momentum, $J(m) = \int_0^m j(m')\,\mathrm{d}m'$, divided by $m^{5/3}$ (thick lines; Panels **E** and **F**) as a function of the mass coordinate m at different evolutionary stages for two $15\,\mathrm{M}_\odot$ stars. The evolution of stars with a ZAMS equatorial rotational velocity of $\sim 100\,\mathrm{km\,s^{-1}}$ (left; Model `G15B`) and and $\sim 300\,\mathrm{km\,s^{-1}}$ (right; Model `F15B`) are depicted. In both models, the effect of μ-gradients on rotational mixing is taken into account. The thin lines in Panels **E** and **F** give a logarithmic scale of levels of constant J, labeled with $\log\,(J/\mathrm{erg\,s})$.

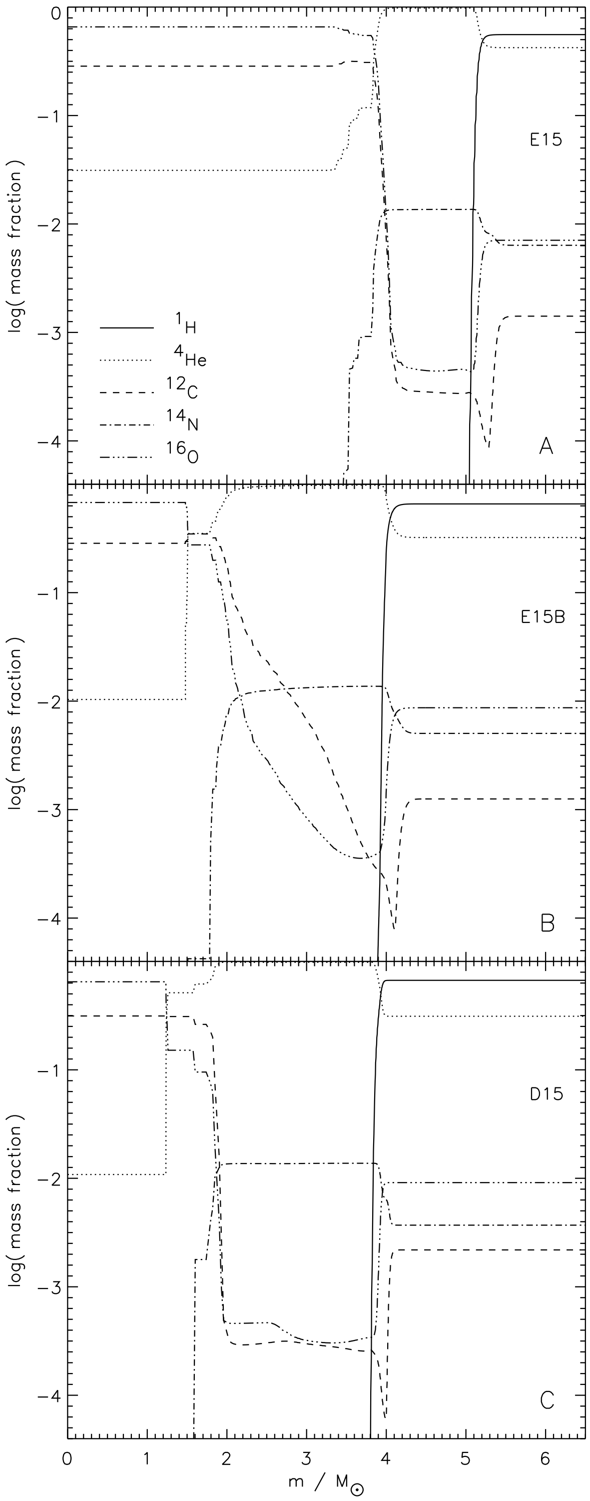

Fig. 10.— Mass fraction of the dominant species of three $15\,\mathrm{M}_\odot$ models at the end of central helium burning as a function of the mass coordinate m. Panels **A** and **B** refer to Models `E15` and `E15B`, respectively, which have a ZAMS equatorial rotational velocity of $\sim 200\,\mathrm{km\,s^{-1}}$, but different assumptions for the parameters of rotationally induced mixing. Panel **C** shows the non-rotating Model `D15`.

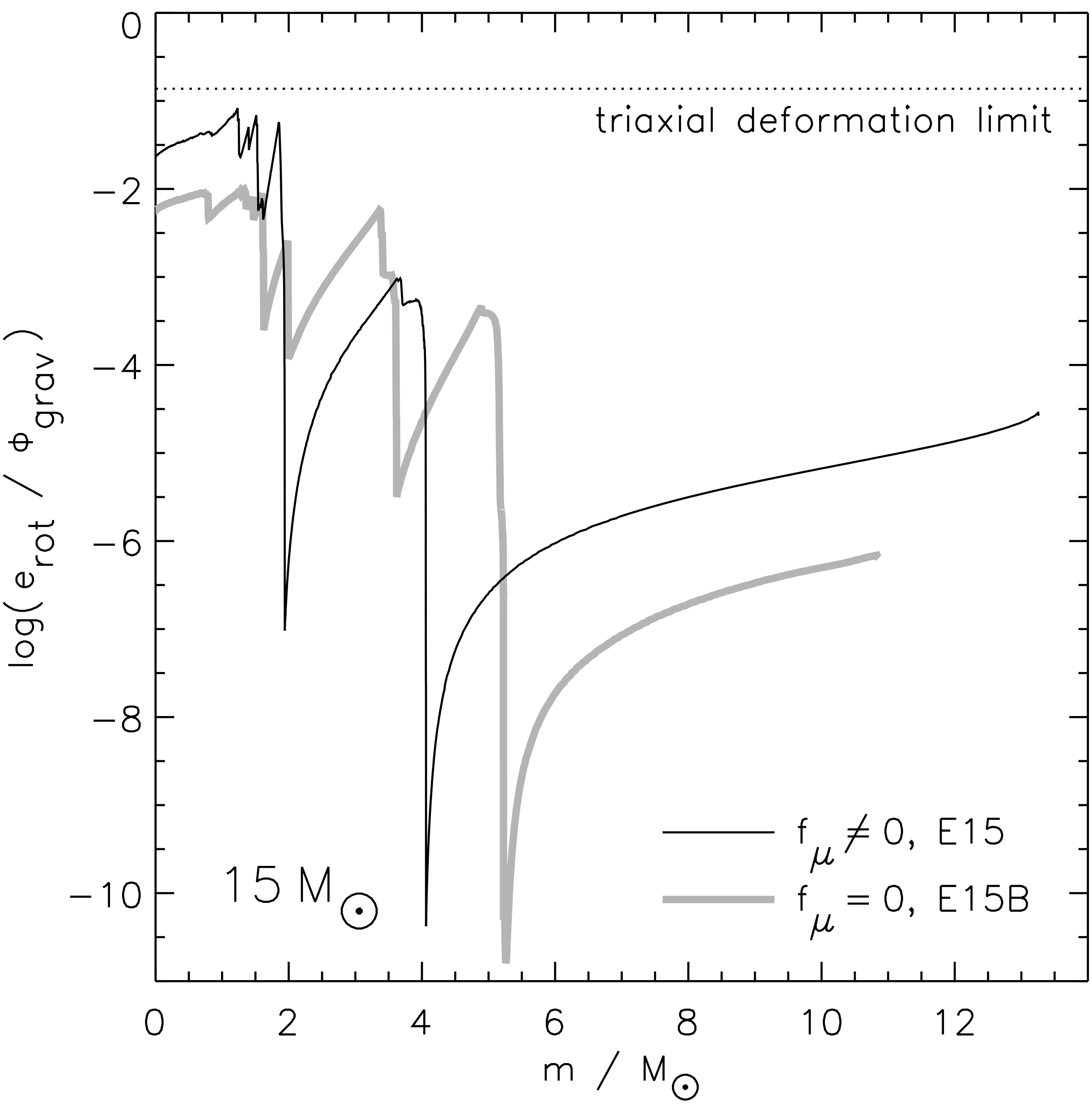

Fig. 11.— Ratio of integrated rotational energy $E_{\rm rot}(m) = \frac{1}{2}\int_0^m \omega(m')j(m')\,\mathrm{d}m'$ to integrated gravitational potential energy $E_{\rm pot}(m) = \int_0^m Gm'/r(m')\,\mathrm{d}m'$ as a function of the mass coordinate m for different $15\,\mathrm{M}_\odot$ stars. The thin solid line corresponds to Model `E15B`, the thick grey line refers to Model `E15`. The dotted line shows the limit for secular instability to triaxial deformations in McLaurin spheroids (Ostriker & Bodenheimer 1973).

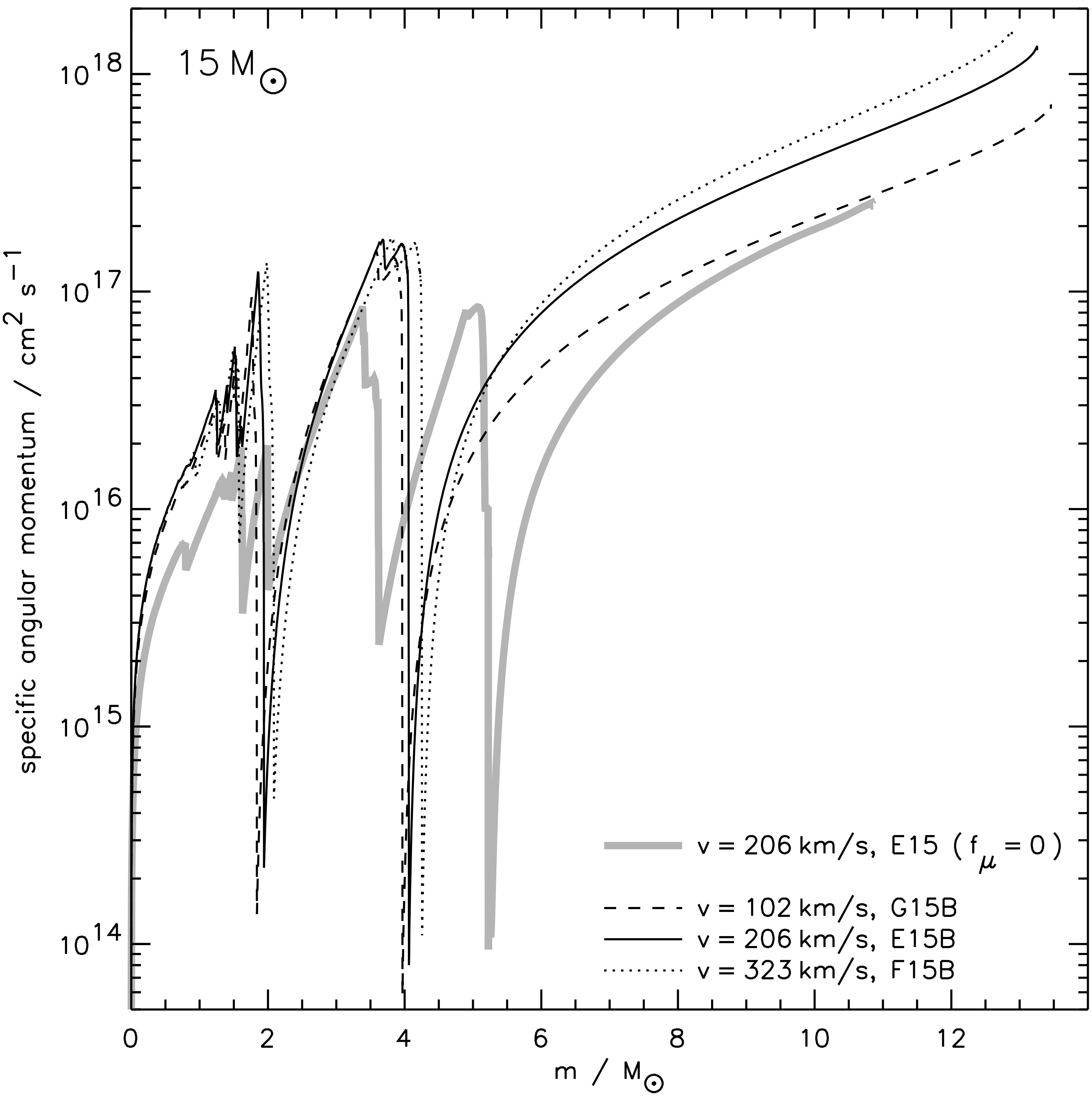

Fig. 12.— Specific angular momentum as a function of the mass coordinate m for $15\,\mathrm{M}_{\odot}$ stars at the onset of core collapse. The thin lines show Models `G15B`, `E15B`, and `F15B` with ZAMS rotational velocity of $\sim 100\,\mathrm{km\,s^{-1}}$ (dotted), $\sim 200\,\mathrm{km\,s^{-1}}$ (solid), and $\sim 300\,\mathrm{km\,s^{-1}}$ (dashed), respectively. The thick grey line shows the Model `E15`.

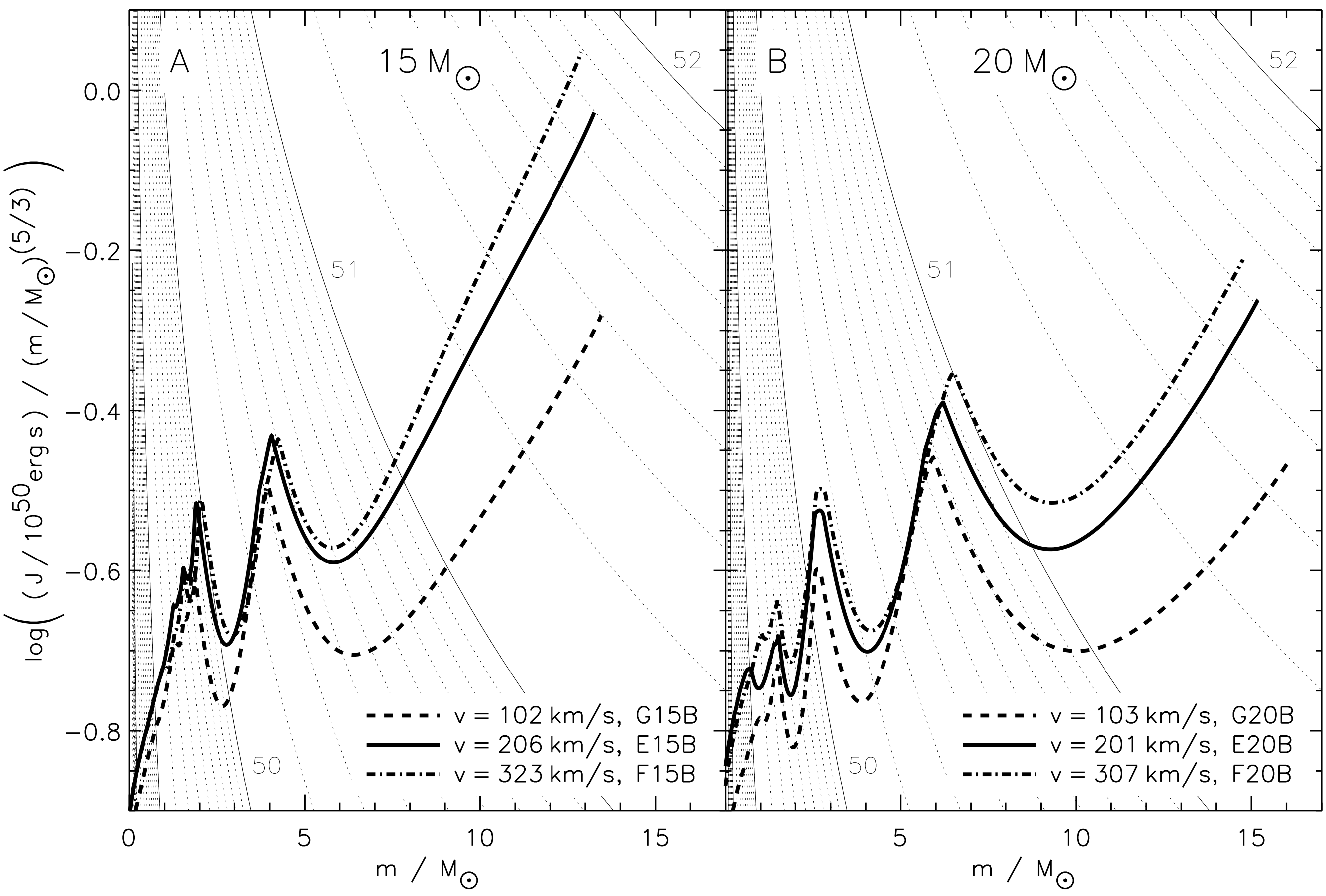

Fig. 13.— Integrated angular momentum $J(m) = \int_0^m j(m')\,\mathrm{d}m'$ divided by $m^{5/3}$ as a function of the mass mass coordinate m for different ZAMS rotational velocities (thick lines) at core collapse. The two Panels show stars of initial masses of $15\,\mathrm{M}_\odot$ (Panel **A**: Models `G15B`, `E15B`, and `F15B`) and $20\,\mathrm{M}_\odot$ (Panel **B**: Models `G20B`, `E20B`, and `F20B`). The thin lines have the same meaning as in Figs. 8E and F.

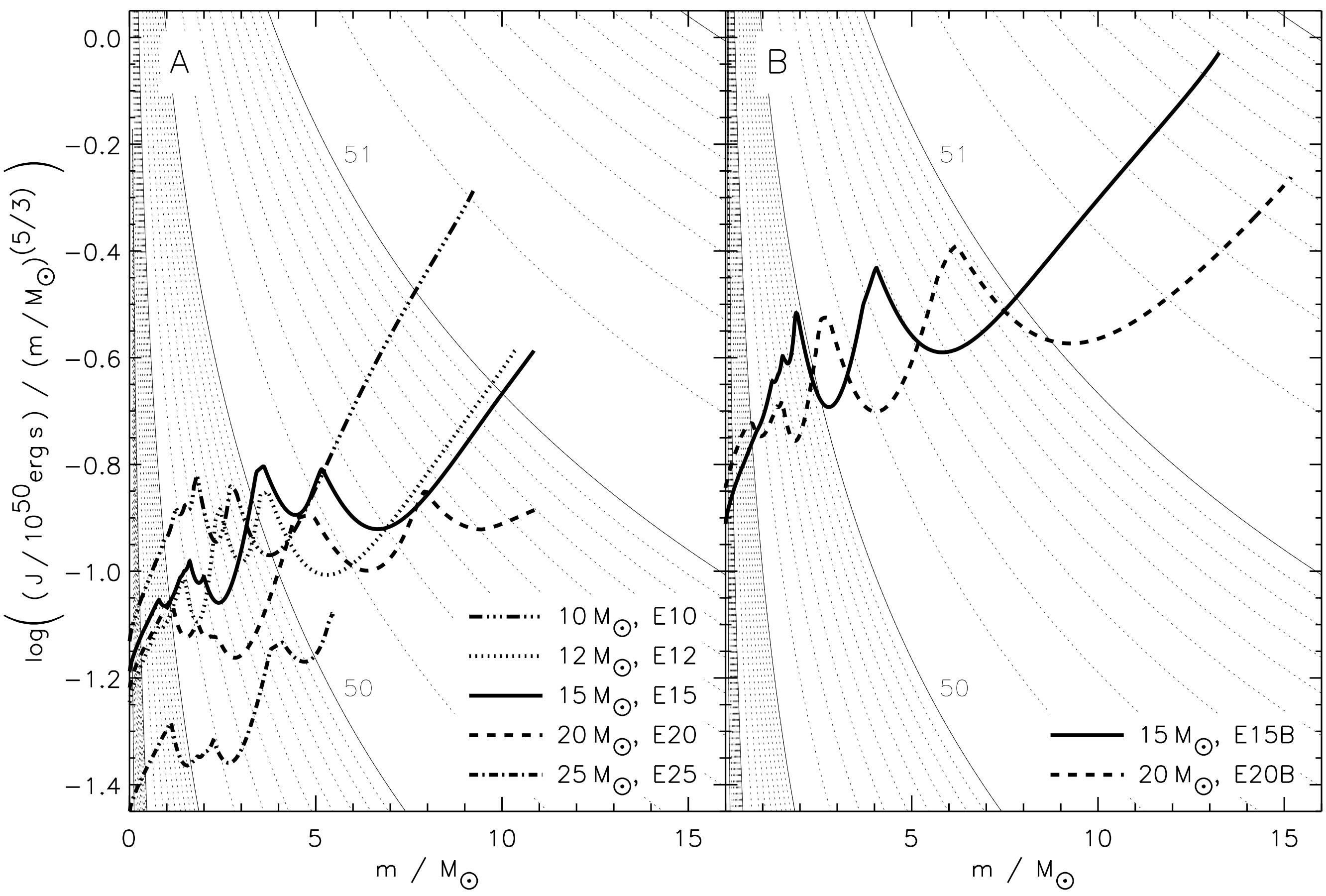

Fig. 14.— Integrated angular momentum $J(m) = \int_0^m j(m')\,\mathrm{d}m'$ divided by $m^{5/3}$ as a function of the mass mass coordinate m for different initial masses (thick lines) at core collapse. The stars have a ZAMS equatorial rotational velocity of $\sim 200\,\mathrm{km\,s^{-1}}$. Panel **A** displays the Models E10, E12, E15, E20, and E25. Panel **B** gives the Models E15B and E20B. The thin lines have the same meaning as in Figs. 8E and F.

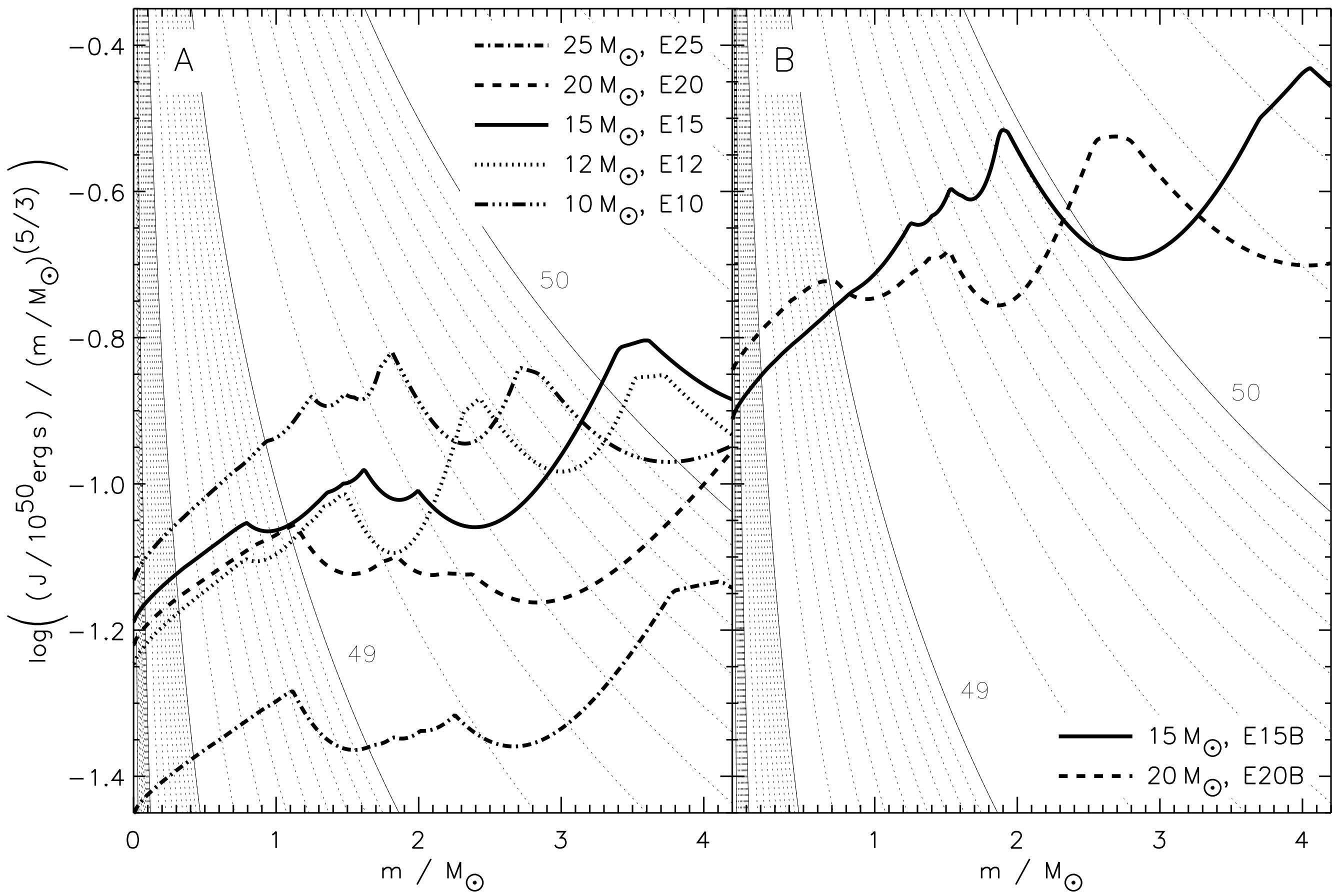

Fig. 15.— Magnification of the innermost $4.2\,\mathrm{M}_\odot$ of Fig. 14.

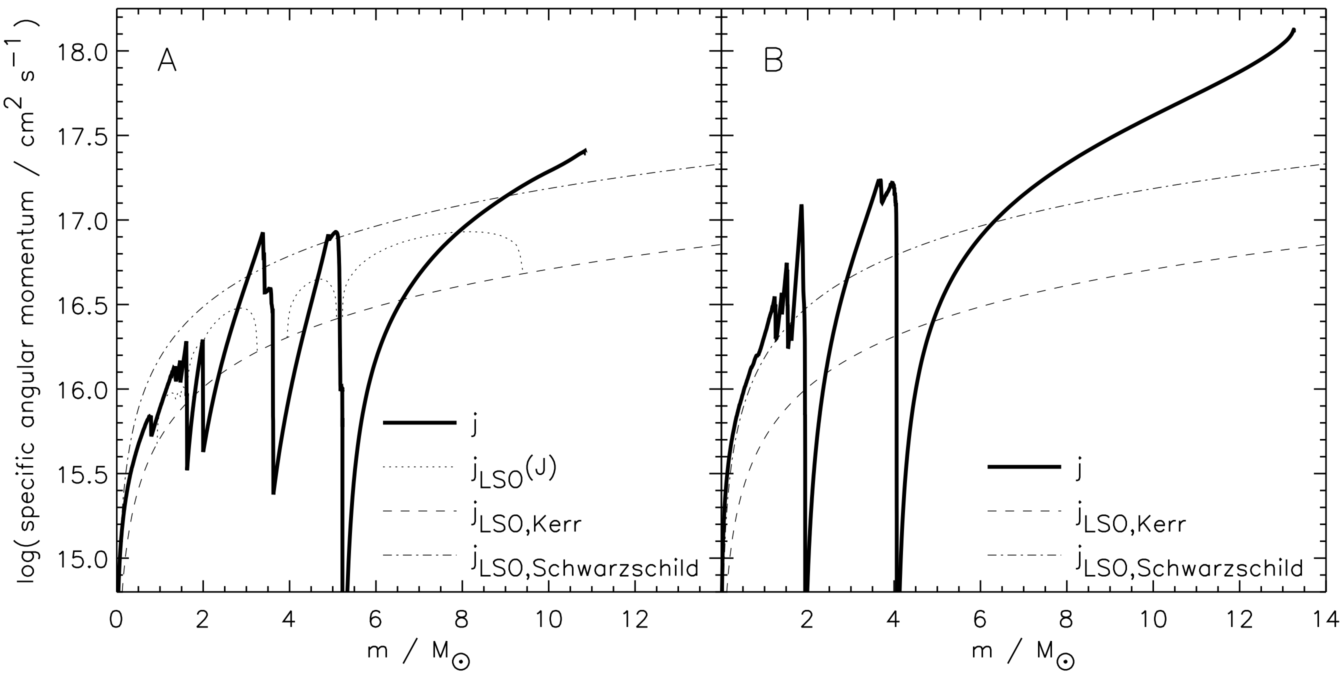

Fig. 16.— Specific angular momentum j in the star (thick line) as a function of the mass mass coordinate m at the onset of core collapse of a $15\,\mathrm{M}_\odot$ star with a ZAMS equatorial rotational velocity of $\sim 200\,\mathrm{km\,s}^{-1}$. Panel **A** and **B** show Models `E15` and `E15B`, respectively, and compare the the resulting profiles of stars with different assumptions about the parameters of rotationally induced mixing. The dash-dotted line gives the specific angular momentum needed to get into the last stable orbit around a non-rotating Schwarzschild black hole of (rest-)mass equal to the mass coordinate. The dashed line give the same but for a maximum-rotating Kerr black hole (spin-parameter $Jc/(Gm) =: a = m$). If assumed that all (rest-)mass below a given m has fallen into a black hole and added its angular momentum to it, the dotted line results for the j needed to get into the last stable orbit; where this approximation would lead to values of $a > m$ the curve is truncated to the Kerr-limit. For the Model `E15B` shown in Panel **B** this is the case everywhere. A derivation of these limits can be found in Shapiro & Teukolski (1983) or Novikov (1997). It has to be noted, however, that this plot is for giving a measure of the amount of angular momentum in the pre-collapse model only. This shall not imply that these stars actually will form black holes.

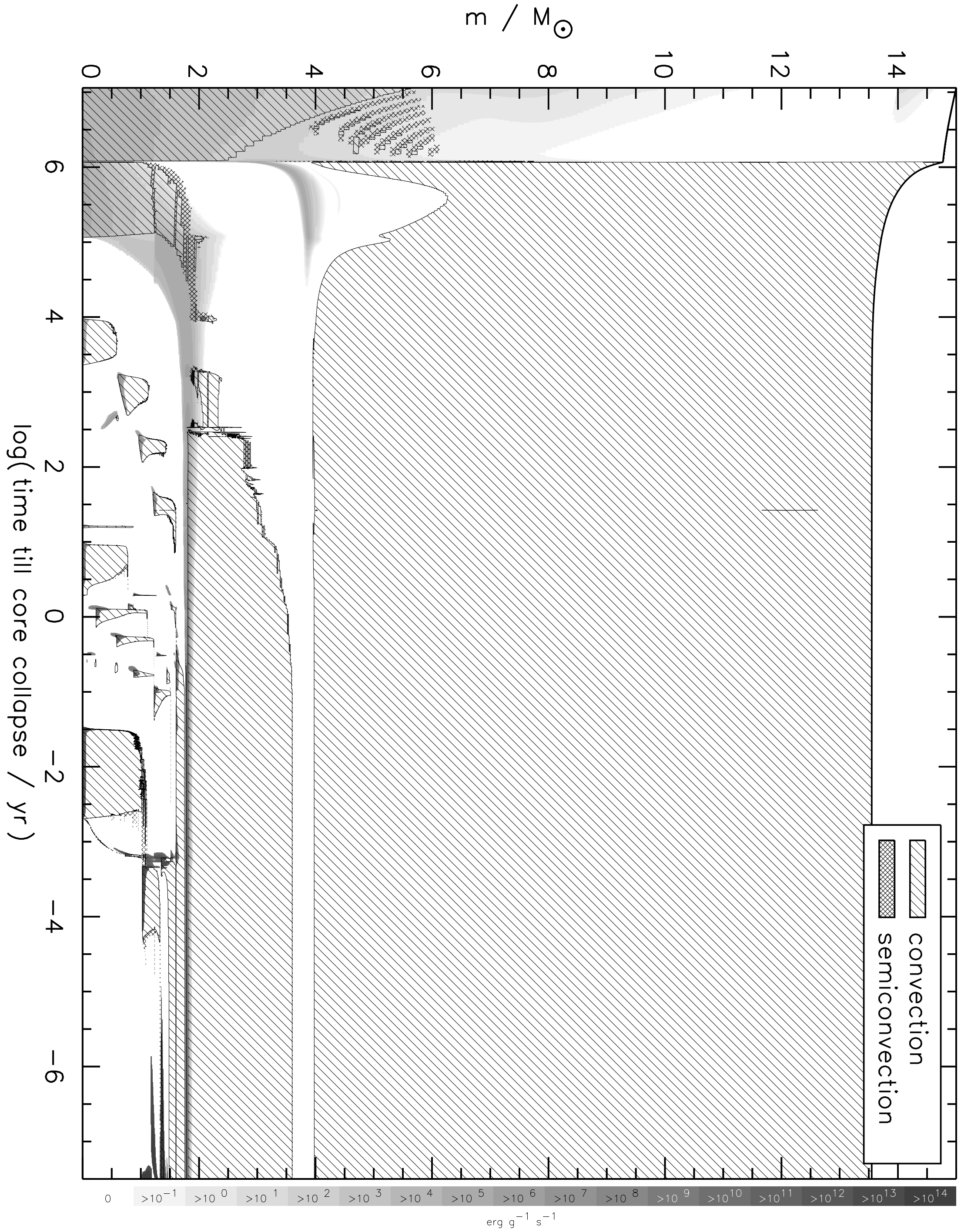

Fig. 17.— Evolution of Model D15 until core collapse. Convection and net nuclear energy generation. See Appendix B for details.

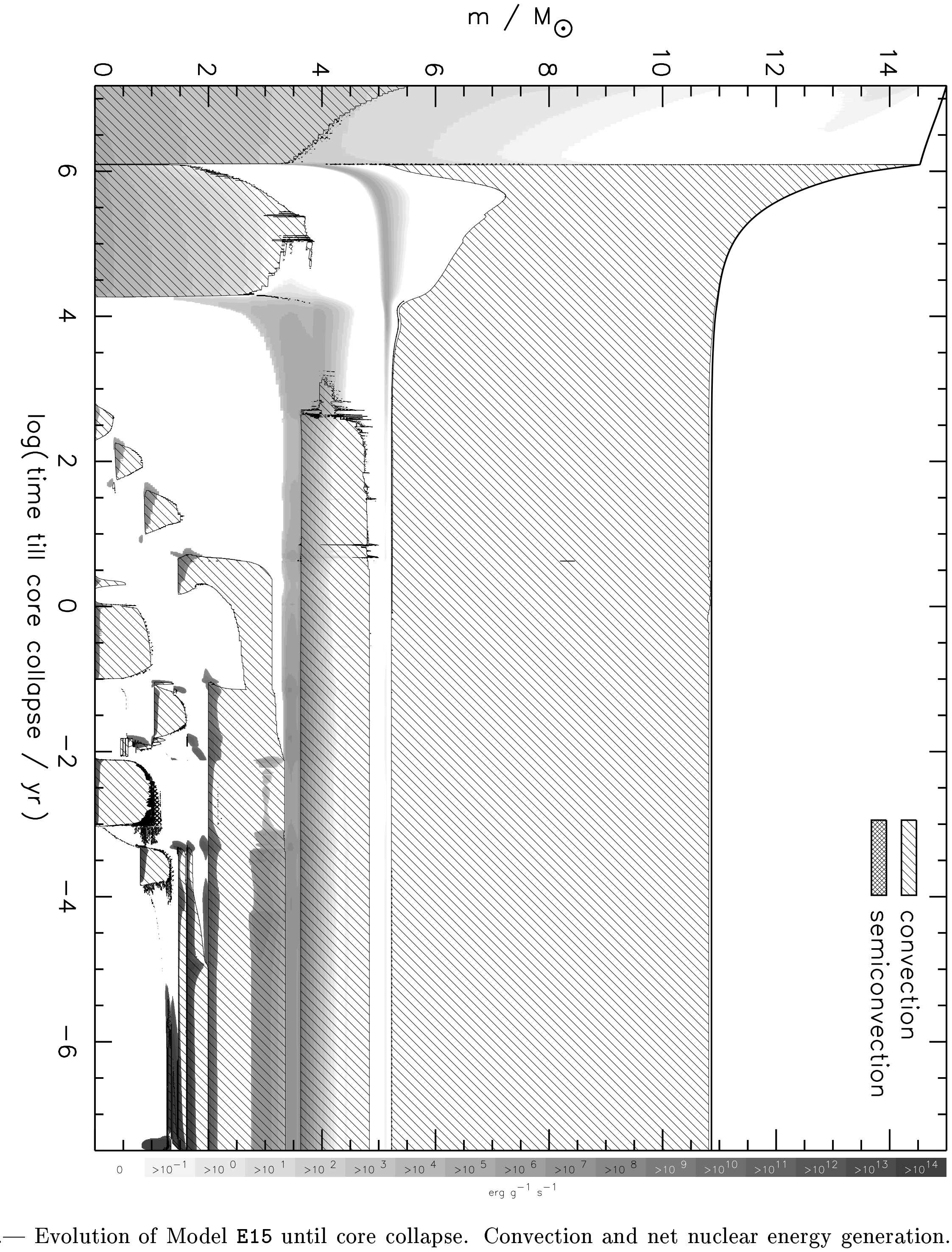

Fig. 18.— Evolution of Model **E15** until core collapse. Convection and net nuclear energy generation. See Appendix B for details.

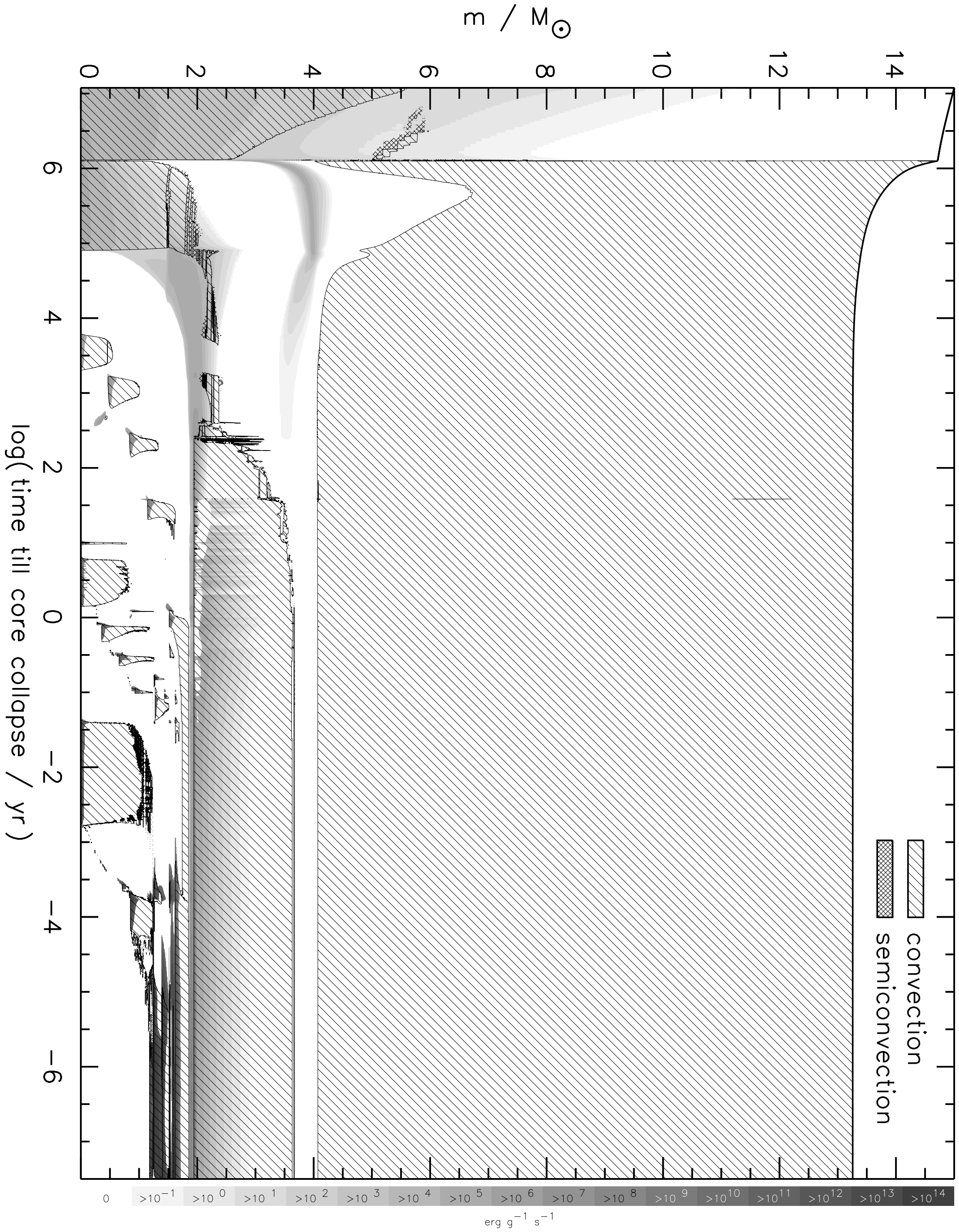

Fig. 19.— Evolution of Model **E15B** until core collapse. Convection and net nuclear energy generation. See Appendix B for details.